



ALMA MATER STUDIORUM  
UNIVERSITÀ DI BOLOGNA

ARCHIVIO ISTITUZIONALE  
DELLA RICERCA

## Alma Mater Studiorum Università di Bologna Archivio istituzionale della ricerca

Mechanical response of dot-by-dot wire-and-arc additively manufactured 304L stainless steel bars under tensile loading

This is the final peer-reviewed author's accepted manuscript (postprint) of the following publication:

*Published Version:*

Mechanical response of dot-by-dot wire-and-arc additively manufactured 304L stainless steel bars under tensile loading / Laghi V.; Palermo M.; Tonelli L.; Gasparini G.; Girelli V.A.; Ceschini L.; Trombetti T.. - In: CONSTRUCTION AND BUILDING MATERIALS. - ISSN 0950-0618. - STAMPA. - 318:(2022), pp. 125925.1-125925.19. [10.1016/j.conbuildmat.2021.125925]

*Availability:*

This version is available at: <https://hdl.handle.net/11585/841748> since: 2024-03-07

*Published:*

DOI: <http://doi.org/10.1016/j.conbuildmat.2021.125925>

*Terms of use:*

Some rights reserved. The terms and conditions for the reuse of this version of the manuscript are specified in the publishing policy. For all terms of use and more information see the publisher's website.

This item was downloaded from IRIS Università di Bologna (<https://cris.unibo.it/>).  
When citing, please refer to the published version.

(Article begins on next page)

This is the final peer-reviewed accepted manuscript of:

Vittoria Laghi, Michele Palermo, Lavinia Tonelli, Giada Gasparini,  
Valentina Alena Girelli, Lorella Ceschini, Tomaso Trombetti

## Mechanical response of dot-by-dot wire-and-arc additively manufactured 304L stainless steel bars under tensile loading

In: Construction and Building Materials, Volume 318, 2022

The final published version is available online at:

<https://doi.org/10.1016/j.conbuildmat.2021.125925>

Rights / License:

The terms and conditions for the reuse of this version of the manuscript are specified in the publishing policy. For all terms of use and more information see the publisher's website.

*This item was downloaded from IRIS Università di Bologna (<https://cris.unibo.it/>)*

***When citing, please refer to the published version.***

# Mechanical response of dot-by-dot Wire-and-Arc Additively Manufactured 304L stainless steel bars under tensile loading

Vittoria Laghi Ph.D<sup>1\*</sup>, Michele Palermo Ph.D<sup>1</sup>, Lavinia Tonelli Ph.D<sup>2</sup>, Giada Gasparini Ph.D<sup>1</sup>,  
Valentina Alena Girelli Ph.D, Lorella Ceschini Ph.D<sup>2</sup>, Tomaso Trombetti Ph.D<sup>1</sup>

\*corresponding author: [vittoria.laghi2@unibo.it](mailto:vittoria.laghi2@unibo.it), ORCID ID: <https://orcid.org/0000-0001-8395-2194>

<sup>1</sup>Department of Civil, Chemical, Environmental and Materials Engineering (DICAM) - University of  
Bologna, Viale del Risorgimento, 2 – 40136 Bologna, Italy

<sup>2</sup>Department of Industrial Engineering (DIN) - University of Bologna, Bologna (Italy)

## Abstract

1 With the advent of a new arc-based additive manufacturing (AM) process, referred to as Wire-and-  
2 Arc Additive Manufacturing (WAAM), the scale of the metal printed parts increased up to several  
3 meters, thus becoming suitable for large-scale applications in marine, aerospace and construction  
4 sectors. However, specific considerations in terms of geometrical and mechanical properties ought to  
5 be made in order to effectively use the printed outcomes for structural engineering purposes. The  
6 introduction of the novel printing strategy referred to as “dot-by-dot”, consisting in successive drops  
7 of molten metal, enabled the use of WAAM for complex lattice structures, made by continuous grids  
8 of WAAM bars. Nevertheless, their proper design requires an accurate evaluation of the influence of  
9 the non-negligible inherent geometrical irregularities on the mechanical response of the bars. Hence,  
10 extensive experimental work is needed in order to evaluate the mechanical response of WAAM bars  
11 with geometrical imperfections.

12 The present study is thus focused on the assessment of the mechanical response in tension of WAAM-  
13 produced 304L stainless steel small bars in terms of key effective mechanical parameters. As such,  
14 the mechanical characterization through tensile tests is supported by microstructural investigations  
15 and detailed studies on the geometrical features. Three batches of bars are studied, each one printed  
16 at different build angles representative of limit cases for practical applications. The microstructural  
17 analysis confirms the preferential grain orientation typical of WAAM process for all three build  
18 angles. The results of the geometrical and mechanical characterization clearly evidence the non-  
19 negligible influence of the inherent geometrical imperfections on the mechanical response in tension  
20 of the printed bars, with a detrimental effect of the build angle on the main key effective mechanical  
21 parameters. Overall, the results highlight the need of specific investigations on both geometrical and  
22 mechanical properties of WAAM bars for structural design purposes.

23

**Key words**

Additive Manufacturing; Wire-and-arc; Stainless steel; Mechanical response; Tensile tests; Microstructural analysis.

## 1. Introduction

1 Among different metal-based Additive Manufacturing (AM) processes, Wire-and-Arc Additive  
2 Manufacturing (WAAM) results to be the most suitable for construction applications to realize large  
3 structural components and real-scale structural elements with ideally no geometrical limitations in  
4 shape and size, while still maintaining good mechanical performances [1–3]. In the last few years,  
5 various research studies focused on the microstructural and mechanical features of different WAAM  
6 processed metals, such as steels [4-16], titanium [17–19] and aluminum alloys [20–23]. Regarding  
7 WAAM of steels, recent studies investigated their mechanical response with specific reference to the  
8 inherent issues proper of the printing process, i.e. the anisotropic nature of the printed parts [5–  
9 8,14,16,24] and the geometrical irregularities which might affect their mechanical behavior [25,26].  
10 The first explorations of WAAM applications in construction were conducted with the layer-by-layer  
11 deposition strategy, to realize planar (shell) elements by deposition of successive layers of molten  
12 metal, see e.g. [27–29]. More recently, an alternative single-cycle deposition strategy (also referred  
13 to as skeleton WAAM [30] and hereafter as “dot-by-dot” deposition) was investigated to realize bars  
14 and lattice elements [31] through the deposition of successive drops of molten metal. Current research  
15 is also investigating the application of the printed bars as steel reinforcement for innovative 3D-  
16 printed concrete structures [32,33]. Nonetheless, given the novelty of the printing strategy, the  
17 reported research activity on this technique is still very limited [34–36].

18 WAAM-produced elements are generally characterized by specific features related to the printing  
19 process which should be properly investigated: (i) different material properties with respect to the  
20 conventional wrought counterpart; (ii) possible anisotropic mechanical behavior with respect to the  
21 printing direction; (iii) geometrical irregularities related to the WAAM deposition strategy (either  
22 layer-by-layer or dot-by-dot). Therefore, it becomes crucial to study WAAM-produced parts from the  
23 microstructural, geometrical and mechanical point of view in order to assess their mechanical  
24 response for structural design purposes.

25 Over the last years, the authors have been studying the microstructural and mechanical features of  
26 WAAM-produced ferrous and non-ferrous metals (304L austenitic stainless steel and 5083 aluminum  
27 alloy) [25,37–42]. With specific focus on the austenitic stainless steel, the results revealed a marked  
28 orthotropic nature, related to the strongly oriented microstructure [40]. The mechanical  
29 characterization highlighted appreciable differences in the tensile response of specimens oriented at  
30 different directions with regard to the printing layers [38]. Moreover, specific studies were carried  
31 out to evaluate the influence of the geometrical irregularities and surface roughness on the mechanical  
32 response of as-built WAAM plates [25].

1 As for the layer-by-layer printed plates, also dot-by-dot printed bars need to be studied in terms of  
2 mechanical response accounting for their inherent geometrical irregularities. Indeed, a typical  
3 WAAM bar has one main building direction and a nominal constant cross-section (corresponding to  
4 the weld drop). Hence, for structural design purposes, it can be ideally assumed as a straight  
5 cylindrical element having circular cross-section with constant along-the-length area, even though  
6 the actual printed outcome is characterized by non-negligible lack of straightness and cross-section  
7 variation, due to the spot-like deposition. Concerning the mechanical behavior, given the bar  
8 geometry and the relatively small cross-section (usually of the order of 5 to 6 mm diameter) of the  
9 specimens to be tested, machining process becomes quite challenging and costly for practical  
10 applications. Hence, specific considerations on both geometrical and mechanical features of as-built  
11 printed bars should be addressed.

12 Another important aspect specific of the dot-by-dot printing process is the relative inclination of the  
13 torch and the nozzle. In this regard, very recently, Silvestru et al. [35] performed an investigation on  
14 WAAM-produced mild steel bars printed at different inclinations of the build angles (e.g. the  
15 inclination of the printed bar with respect to the vertical gravity axis) and nozzle angles (e.g. the  
16 inclination of the nozzle with respect to the printed bar) by means of 3D laser scanning, tensile tests  
17 and non-linear finite element analysis. The results of the study indicated that both the built angle and  
18 the nozzle angle have a detrimental effect on the geometrical irregularities (variation along the length  
19 of the cross-sectional area), while they did not provide a significant effect on the mechanical  
20 properties as evaluated on machined specimens. On the other hand, the as-built bars evidenced non-  
21 negligible reduction on strength, elongation and ductility.

22 This study aims at providing the first results on an extensive work devoted to assess the mechanical  
23 response of WAAM stainless steel bars for structural design purposes. In particular, the study here  
24 presented is focused on the mechanical response in tension of single bars printed at three different  
25 build angles. The results are aimed at evaluating the influence of both build angle and geometrical  
26 irregularities (proper of the selected printing process) on the mechanical properties. For this purpose,  
27 detailed geometrical characterization is carried out on two levels: (i) a specimen-to-specimen  
28 characterization to assess the variability of the geometry within the same batch, and (ii) an inherent  
29 characterization on the single bar to assess the variability of the geometry along the element.  
30 Additional microstructural investigations are also provided through conventional metallographic  
31 analyses, based on the use of optical and scanning electron microscopy. The mechanical response is  
32 then estimated through tensile tests on as-built bars to assess the key effective mechanical parameters  
33 of WAAM bars useful for structural design purposes.

1 The paper is organized as follows. Section 2 provides the problem formulation by introducing the key  
2 aspects influencing the mechanical response of a bar with imperfections through a simple mechanical  
3 model. The aim is to highlight, from a qualitative point of view, the potentially major influence of  
4 both geometrical irregularities and material constitutive behavior on the global force-elongation  
5 response of steel bars with imperfections. Section 3 illustrates the aim and the methods adopted to  
6 carry out the experimental tests, whose results are reported in Section 4. Section 5 provides an  
7 interpretation of the mechanical response of WAAM bars based on the experimental results. Some  
8 concluding remarks and recommendations are finally drawn.

9

## 2. Problem formulation of the mechanical response of a steel bar with geometrical imperfections

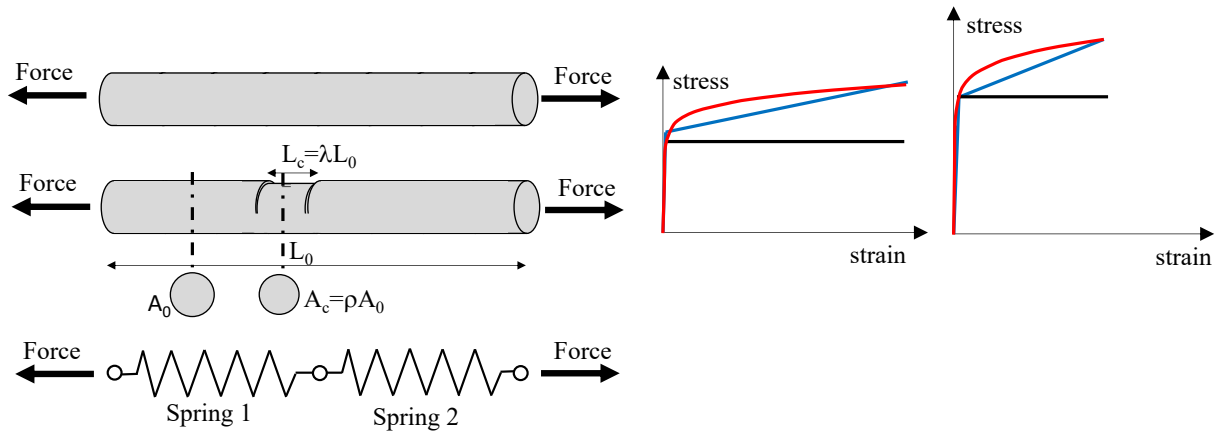
### 2.1 General case of a steel bar with geometrical imperfections

1 Generally speaking, the mechanical behavior of a steel bar can be severely affected by the presence  
2 of geometrical imperfections (e.g. cross-sectional variations along the longitudinal axis), especially  
3 when considering ultimate deformation capacity. A relevant example is represented by the  
4 phenomenon of the pitting corrosion of prestressing strands and rebars that may cause severe  
5 reductions of ultimate strength and deformation capacities [43–45] up to catastrophic failure (e.g.  
6 Polcevera bridge in Northern Italy [46,47]). In fact, in such case the axial stress field induced by an  
7 external axial load is not uniform along the element length and local stress concentrations and early  
8 plasticization may occur with the remaining part still in the elastic phase. This leads to premature  
9 failure with limited ductility capacity. The influence of local stress concentration and plasticization  
10 in the global force-elongation capacity of the single bar strictly depends on the specific type of  
11 geometrical imperfections and on the material constitutive model [48].

12 For a first appraisal of the influence of these aspects on the tensile response of a steel bar with a  
13 geometrical defect, an element of length  $L_0$  with an idealized defect is considered. The ideal defect is  
14 localized in a portion of length  $L_c$  (which can be described by the dimensionless parameter  $\lambda=L_c/L_0$ )  
15 characterized by a reduced cross-sectional area  $A_c$  (which can be described by a dimensionless  
16 parameter  $\rho=A_c/A_0$ , where  $A_0$  indicates the cross-sectional area of the defect-free bar). At first  
17 approximation, the damaged element can be modelled by two non-linear springs connected in series.  
18 The graphs of Figure 1 reproduce the qualitative force-elongation behavior of the whole damaged  
19 element as compared to the corresponding undamaged one. The behavior is studied by considering  
20 three different constitutive models: an elastic-perfectly plastic (EPP) model, an elasto-plastic with  
21 hardening (EPH) model and a non-linear Ramberg-Osgood (RH) [49] model. Two different steel  
22 types are also considered: low-strength/high-ductility steel and high-strength/low-ductility steel ( $\mu_m$   
23 indicates the material ductility).

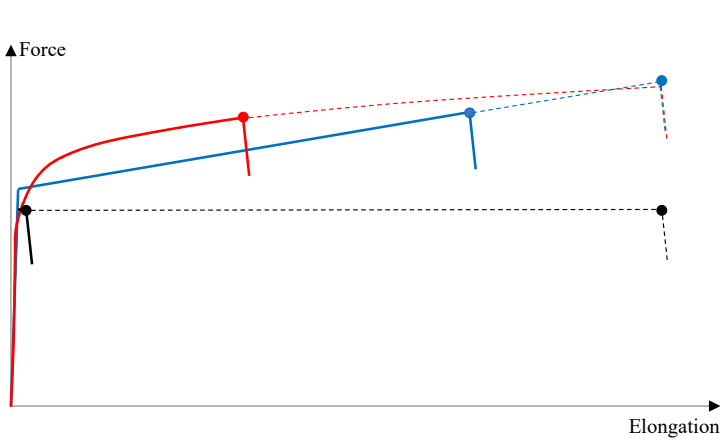
24



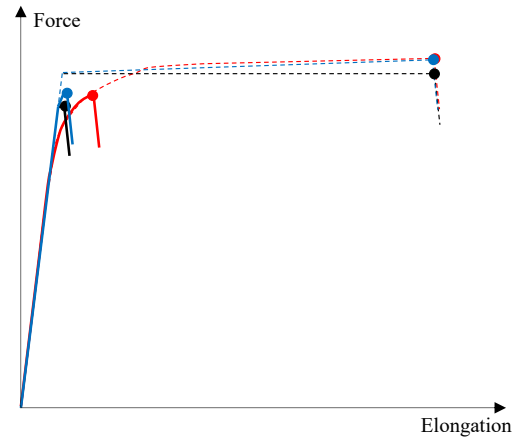


(a)

-- Ideal (EPP)    -- Ideal (EPH)    -- Ideal (RH)  
 - With defect (EPP)    - With defect (EPP)    - With defect (RH)



(b)



(c)

Figure 1: (a) Mechanical model of a bar with geometrical imperfections; Force-elongation of a metal bar with a single geometrical defect (characterized by  $\rho=0.9$  and  $\lambda=0.01$ ) for (b) high-ductility ( $\mu_m=100$ ) material behavior and (c) low-ductility ( $\mu_m=10$ ) material behavior.

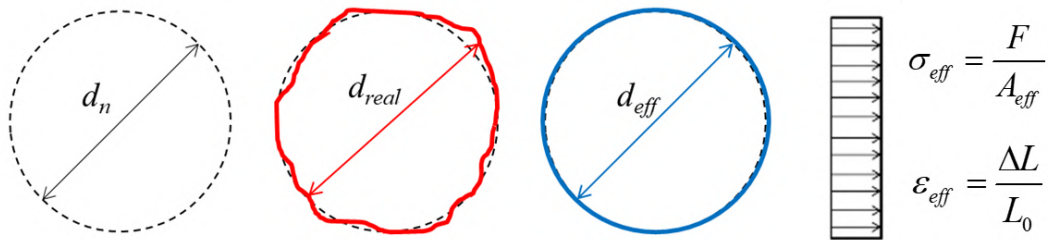
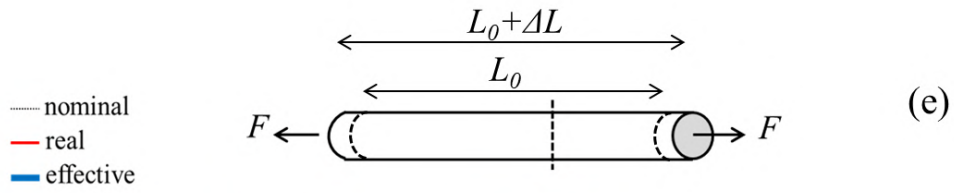
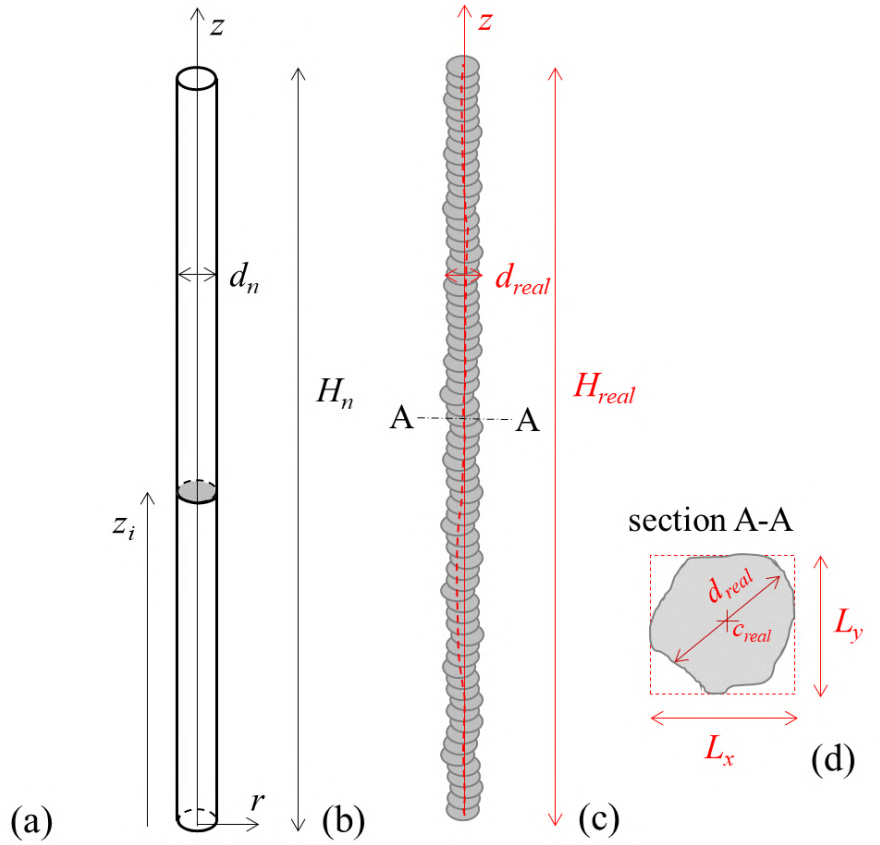
Fig.1 b and c clearly show the very large variability of the force-elongation behavior in tension due to the coupling of geometrical irregularities and non-linear material constitutive behavior. Hence, from a structural design point of view it becomes of high interest to assess the whole element's response when subjected to tensile force with specific focus on the influence of the geometrical irregularities.

For the present study, the WAAM bars are studied at a macro scale through geometrical and mechanical characterization to derive the effective stresses and strains evaluated from the whole force-elongation response.

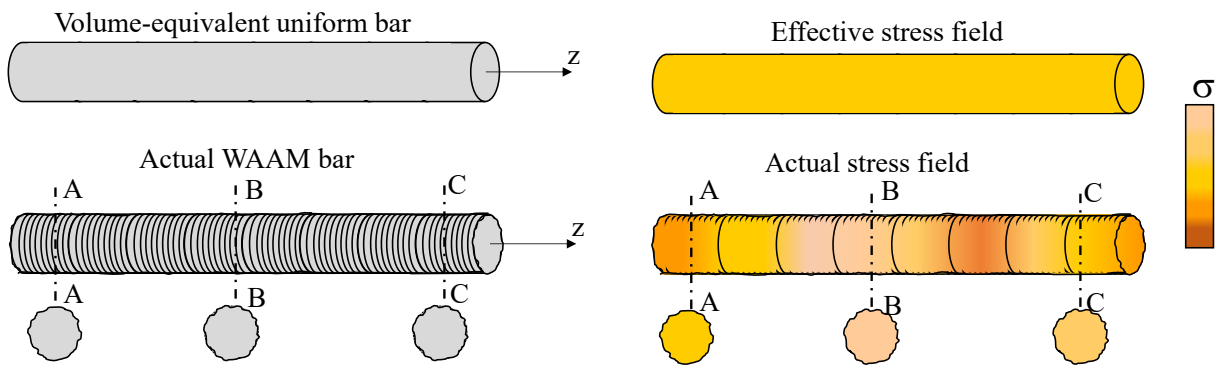
## 2.2 Specific case of WAAM bars

1 Dot-by-dot printed elements are produced through successive deposition of metal droplets along the  
2 main axis ( $z$ -axis). This results in 3D elements (bars) of constant nominal diameter directly related to  
3 the drop of liquid metal, with one main growing direction. Usually, for current printing technologies  
4 the nominal diameter of WAAM bars varies within the range of 4 to 8 mm [50]. However, for dot-  
5 by-dot printed bars the successive deposition of metal droplets causes a variation of their real diameter  
6 along the height of the bar of the order of around 0.5 mm, resulting in a visible surface roughness,  
7 similarly to the one generated by the layer-by-layer deposition for continuously-printed plates [25].  
8 Additionally, the deposition process can also induce some lack of straightness due to inaccurate  
9 positioning of the torch, which should also be investigated (Figure 2a). Hence, with regards to dot-  
10 by-dot WAAM bars, the deposition strategy results in a non-uniform circular cross-section and non-  
11 straight longitudinal axis (formed by the polyline connecting the centroids of each circular cross-  
12 section).

13 The nominal geometry of the digital model for the investigated WAAM bars consists in a uniform  
14 full cylinder with straight longitudinal axis (coincident with  $z$ -axis of the cylindrical coordinate  
15 system, Figure 2b). The geometry is described by the nominal bar height ( $H_n$ ) and the nominal cross-  
16 sectional diameter ( $d_n$ ). The real geometry of a WAAM bar is, instead, more complex and can be  
17 described by a solid element with non-uniform circular cross-section varying along its length and a  
18 non-straight longitudinal axis (Figure 2c). The coordinate system adopted for the geometrical  
19 description has the origin in the centroid of the base cross-section (e.g.  $C(z=0)$ ) and the  $z$ -axis  
20 corresponding to the one connecting the centroid of the base cross-section and the one of the top  
21 cross-section (e.g.  $C(z=H)$ ).



1



2

(f)

Figure 2: (a) Close-up view of the geometrical description of WAAM bars (printed at 45° and 0° build angle, respectively; bars printed at 10° build angle resulted similar to those at 0°, hence not included); (b) digital model and (c) corresponding printed element of a WAAM bar and (d) detail of one real cross-section; (e) nominal, real and effective cross-sections of the WAAM bar. (f) effective vs actual (true) stress fields.

As a consequence of these geometrical irregularities, it is clear that a detailed description of the mechanical tensile response of the real WAAM bar would require the evaluation of local true stress and strain values. These values vary along the longitudinal axis due to the variation of the cross-sectional area along the length of the bar ( $A=A(z)$ ) and due to the presence of small eccentricities due to the lack of straightness, possibly inducing also additional bending stresses (Figure 2f). Such detailed evaluation would require ad-hoc measurements during experimental tests (e.g. with the use of optical monitoring systems) and complex digital twins, see e.g. [3,27].

As an alternative, from a structural design point of view, the mechanical response of the entire real WAAM bar could be described in terms of effective mechanical parameters (e.g. effective stresses and strains) which are associated to the effective volume-equivalent cross-sectional area  $A_{eff}$  uniform along the whole length of the element as follows:

$$\sigma_{eff} = \frac{F}{A_{eff}} \quad (1)$$

$$\varepsilon_{eff} = \frac{\Delta L}{L_0} \quad (2)$$

Clearly, such effective parameters could be adopted for the design of WAAM bars having the same geometrical properties and realized with the same printing parameters as the ones studied hereafter.

### 3. Experimental tests on WAAM bars

#### 3.1 *The aim and approach*

1 The aim of the experimental work is to assess the mechanical response of WAAM bars for structural  
2 design purposes. From the mechanical point of view, the response is studied under different loading  
3 conditions: tension, compression and bending. The tests are carried out on as-built bar, considering  
4 the real conditions at which they will be subjected for construction applications (i.e. with no post-  
5 processing milling treatments). The results of the experimental tests are then interpreted in terms of  
6 effective quantities (i.e. effective stresses and strains) accounting for the variability and possible  
7 detrimental effects associated to the inherent geometrical irregularities. Detailed microstructural  
8 analyses are also carried out to highlight the microstructure features of WAAM dot-by-dot stainless  
9 steel, also considering possible defects.

The present study is focused on the results of tensile tests carried out on WAAM bars by estimating:  
(i) the geometrical irregularities of both the single specimen (inherent variability) and of the entire  
batch (specimen-to-specimen variability), (ii) the microstructural features proper of the selected  
printing process, (iii) the effective mechanical parameters for structural design purposes. Table 1  
summarizes the specimens' characteristics and tests.

In order to account for the possible influence of the printing direction (with respect to the vertical  
axis) on the overall mechanical response of the printed bars, three different build angles (b-a) are  
considered, consisting in the angle between the axis of the WAAM bar ( $z$ -axis) and the vertical axis  
(perpendicular to the base platform). The nozzle angle (n-a), consisting in the angle between the axis  
of the WAAM bar ( $z$ -axis) and the nozzle axis, was set equal to  $0^\circ$  for all batches. In detail, the  
specimens were printed with build angles equal to  $0^\circ$  (dot-0),  $10^\circ$  (dot-10) and  $45^\circ$  (dot-45) (Figure  
3). The case of  $0^\circ$  and  $45^\circ$  build angles correspond to the common limit conditions ( $0^\circ$  and  $45^\circ$ ) for  
practical applications. The case of  $10^\circ$  build angle corresponds, instead, to a commonly adopted value  
for lattice structural elements (see e.g. [31]).

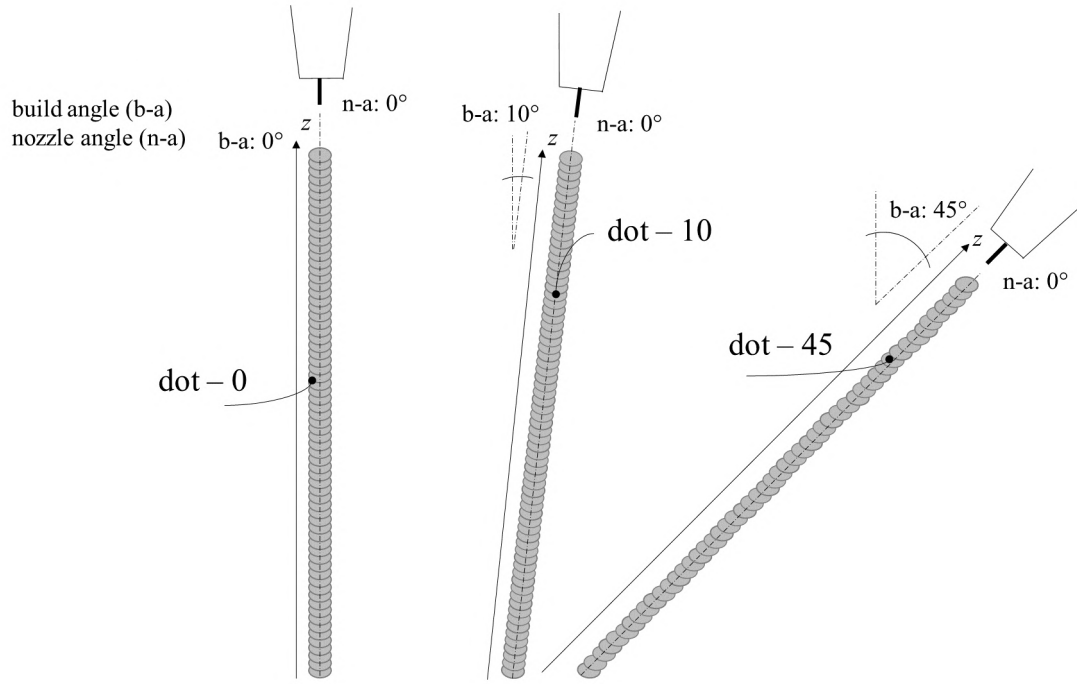


Figure 3: Graphical representation of the WAAM bars printed with three different build angles ( $b-a$ ):  $0^\circ$  (dot-0),  $10^\circ$  (dot-10) and  $45^\circ$  (dot-45).

Table 1: Summary of specimens' characteristics and tests.

Build angle	Specimen ID	Nominal length	Nominal diameter	Geometrical characterization	Mechanical characterization	Quantity
$0^\circ$	dot-0	$H_n=250$ mm	$d_n=6$ mm	Hand Volume 3D scan	Tensile	10
$10^\circ$	dot-10	$H_n=250$ mm	$d_n=6$ mm	Hand Volume	Tensile	10
$45^\circ$	dot-45	$H_n=200$ mm	$d_n=6$ mm	Hand Volume 3D scan	Tensile	9

### 3.2 Material and process

The WAAM bars studied in the present work were produced by MX3D [51] with Gas Metal Arc Welding (GMAW). A commercially-available ER308LSi stainless steel welding wire (1 mm diameter) grade, supplied by Oerlikon [52], was used as feedstock wire. The nominal chemical

1 composition of the wire is reported in Table 2. Welding speed and wire feed rate were 15-30 mm/s  
2 and 4-8 m/min, respectively. The employed shield gas was 98% Ar and 2% CO<sub>2</sub> at a flow rate of 10-  
3 20 L/min, the current and arc voltage of the deposition process were 100-140 A and 18-21 V  
4 respectively, while the deposition rate was 0.5-2 kg/h. Values of the process parameters are provided  
5 within typical ranges adopted by MX3D. For further information the interested reader could refer  
6 directly to MX3D. The substrate was a printing plate of 1000 x 1000 x 30 mm, with welded H-type  
7 beams as support.

### 3.3 *Chemical and microstructural characterization*

8 The chemical composition of WAAM bars was verified by Glow Discharge Optical Emission  
9 Spectroscopy (GDOES), with a sputtered burnt spot of 2.5 mm diameter. Microstructural  
10 characterization was then carried out in order to relate the mechanical parameters to the  
11 microstructural features typical of additively manufactured parts. Samples for microstructural  
12 characterization were extracted from dot-0, dot-10 and dot-45 bars. In the analyses, two directions  
13 were considered: the longitudinal one (i.e. parallel to the *z*-axis, as defined in Figure 2) and the  
14 transverse one (i.e. perpendicular to the *z*-axis). Metallographic sections were embedded in a phenolic  
15 resin and polished up to a mirror finish by following standard metallographic preparation techniques  
16 [53]. Chemical etching with 20 s immersion at ambient temperature in Vilella's reagent (1 g picric  
17 acid, 5 mL hydrochloric acid and 100 mL ethanol [54]) was adopted to reveal general microstructural  
18 features. The presence of ferrite was then confirmed using a specific color etching, described in [55].  
19 Etched metallographic sections were observed by means of optical and field emission gun scanning  
20 electron microscopy (FEG-SEM). An energy-dispersive spectroscopy (EDS) system, available inside  
21 the FEG-SEM microscope, was employed for semi-quantitative compositional microanalyses. In  
22 addition, to further investigate fracture path and failure mechanisms, also samples extracted along the  
23 longitudinal axis of bars, in a region close to the fracture surface, were subjected to the same  
24 metallographic preparation described above and then observed with an optical microscope.

25

### 3.4 *Geometrical characterization*

26 Given the non-uniform cross-section and not-perfectly-straight longitudinal axis, the geometrical  
27 characterization consisted in: (i) evaluating the real cross-sectional area along the longitudinal axis;  
28 (ii) identifying the shape of each cross-section (if it can be assumed as circular at first approximation);  
29 (iii) identifying the real longitudinal axis (corresponding to the polyline connecting the real cross-

1 sectional centroids); (iv) evaluating the volume-equivalent cross-section (for the evaluation of the  
2 effective stresses).

3 First, the specimen-to-specimen geometrical variability was assessed for all specimens then tested  
4 under tensile loading condition. For each of them, the estimation of the volume-equivalent, or  
5 effective, cross-sectional area ( $A_{eff}$ ) of each specimen was taken by means of volume measurements,  
6 based on the Archimedes' principle, as also adopted in [25,26]. From them, the effective diameter is

7 computed as  $d_{eff} = \sqrt{\frac{4A_{eff}}{\pi}}$  (Figure 2e). The measures were taken for each entire specimen before

8 testing. This procedure was previously applied for as-built specimens taken from WAAM-produced  
9 plates, as also presented in [25,26].

10 Then the local geometrical measurements were performed through 3D scanning technique  
11 considering two WAAM bars (printed at  $0^\circ$  and  $45^\circ$  build angles). From the 3D model, a total of 120  
12 cross-sections (equally spaced at 2 mm) along the length of each specimen were extracted, from  
13 which information regarding the cross-sectional diameter and centroid was analyzed. A structured-  
14 light projection Artec Spider 3D scanner [56] was used for the 3D scan acquisition. The 3D model of  
15 the scanned bar consisted of around 40 million triangular elements, with a medium-points spacing of  
16 about 0.10 mm.

17 In detail, for each considered cross-section (located at height  $z$ ) of the real WAAM bar, the cross-  
18 sectional area  $A_{real} = A_{real}(z)$  and the corresponding centroid  $C_{real} = C_{real}(z)$  were measured. In addition,  
19 from the cross-sectional area  $A_{real}$  an equivalent cross-sectional diameter was identified as follows:

20  $d_{real} = \sqrt{\frac{4A_{real}}{\pi}}$ . The equivalent real diameter  $d_{real}$  was computed considering that the shape of the

21 cross-section is close to that of a circle. This assumption is in line with the digital input model used  
22 for the printed bars (see Section 2.2). The discrepancies from the circular shape were computed  
23 comparing the values of the two sides of the circumscribed rectangle ( $L_x$ ,  $L_y$ ) with the equivalent  
24 diameter  $d_{real}$  (see Figure 2c). Then, the identification of the real longitudinal axis was performed by  
25 connecting the centroids  $C_{real}$  (corresponding to the center of mass of each cross-section) of all  
26 sections.

27

### 3.5 Mechanical characterization

28 The tensile tests were performed on a universal testing machine of 500 kN load capacity at the  
29 Structural Engineering labs of University of Bologna.



1 The tensile specimens were tested under displacement control with a velocity corresponding to a  
2 stress rate of 2 MPa/s according to [57]. A linear deformometer (50 mm gauge length) was adopted  
3 to detect the effective strain of the specimens up to yielding (Figure 4).

4



5  
6 (a)

(b)

7 *Figure 4: (a) Tensile test set-up; (b) typical tensile failure for a dot-0 specimen.*

The tensile tests were performed on a total of 29 specimens (10 at 0° build angle, 10 at 10° build angle and 9 at 45° build angle). Elastic Modulus ( $E$ ), 0.2% proof stress ( $Rp_{0.2}$ ), ultimate tensile strength ( $UTS$ ), elongation to failure ( $A\%$ ) and element's ductility ( $\mu_e$ ) were evaluated from the effective stress-strain curves. After the tensile tests, fracture surfaces were analyzed at low magnification by means of a 3D digital microscope and by FEG-SEM, coupled with EDS, for a high magnification investigation.

Vickers hardness measurements ( $HV_1$ ) with a 1 kg load and 15 s dwell time were performed on polished sections extracted from the WAAM bars along the direction parallel and perpendicular to the  $z$ -axis.

1

## 4. Main experimental results

### 4.1 Compositional analysis

Chemical composition evaluated by GDOES on the printed bars is reported in Table 2 and compared to the nominal composition of the feedstock wire. As the 308L Si wire is commonly adopted for the conventional welding of the AISI 304L (UNS-S-30403) austenitic stainless steel, results were also compared to the reference composition of the latter. Apart from a small difference in the Cr content, the chemical composition of the printed bars fulfilled the specifications for the AISI 304L. An analogous outcome was also found for the case of WAAM plates printed with the same wire [38]. Therefore, as the final goal of WAAM is the fabrication of large structural parts, mechanical properties of WAAM bars are hereafter compared to the requirements reported for the AISI 304L in the European Building Code [58] for the design of steel structures.

1 *Table 2: Chemical composition (wt.%) measured on the WAAM bars compared to the nominal chemical*  
2 *compositions of the wire (given by the supplier, and the 304L (UNS-S-30403) austenitic stainless steels [59]*

	<i>C</i>	<i>Cr</i>	<i>Ni</i>	<i>Mn</i>	<i>Si</i>	<i>Co</i>	<i>V</i>	<i>Mo</i>	<i>Cu</i>	<i>P</i>	<i>S</i>	<i>Fe</i>
<b>Feedstock Wire</b>	0.02	20.00	10.00	1.80	0.85	-	-	0.2	-	<0.025	<0.020	Bal.
<b>WAAM bars</b>	0.01	20.17	9.59	1.23	0.94	-	0.11	0.05	0.03	0.043	0.022	Bal.
<b>AISI 304L</b>	<0.03	18.0-20.0	8.0-12.0	<2.0	<1.0	-	-	-	-	<0.045	<0.03	Bal.

According to the Schaeffler diagram [60] and based on the  $Cr_{eq}$  and  $Ni_{eq}$  obtained from the chemical composition of bars, both  $\gamma$ -austenite and  $\delta$ -ferrite (approx. 15 vol.%) phases were expected (Figure 5).

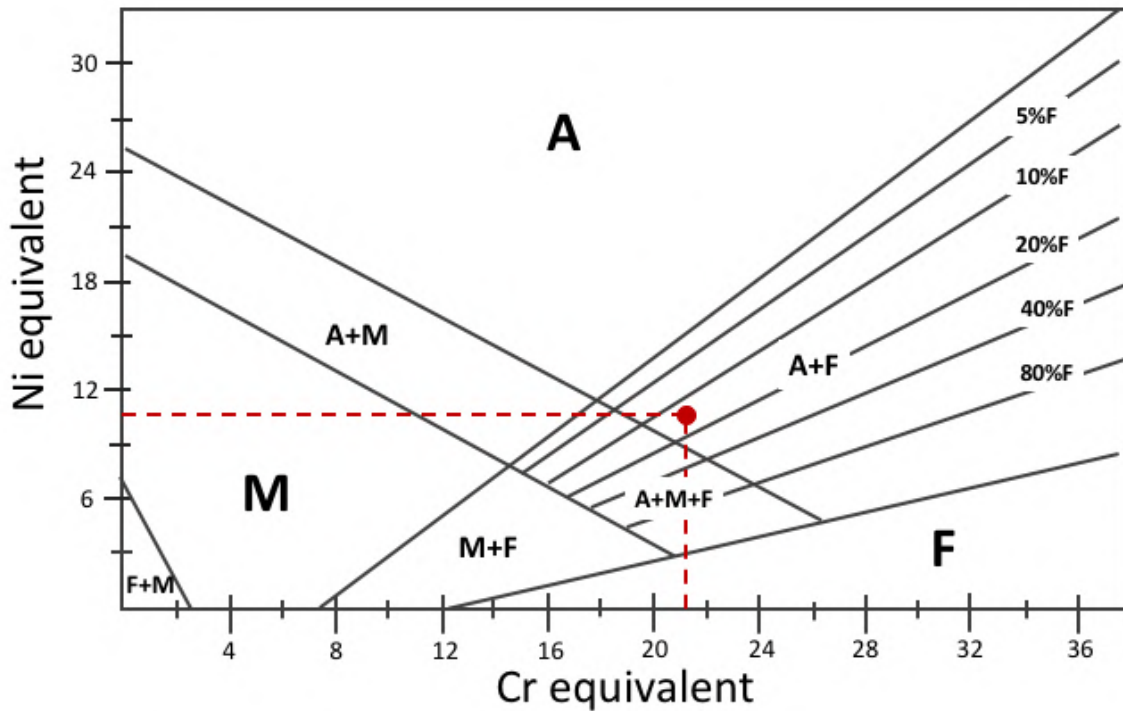
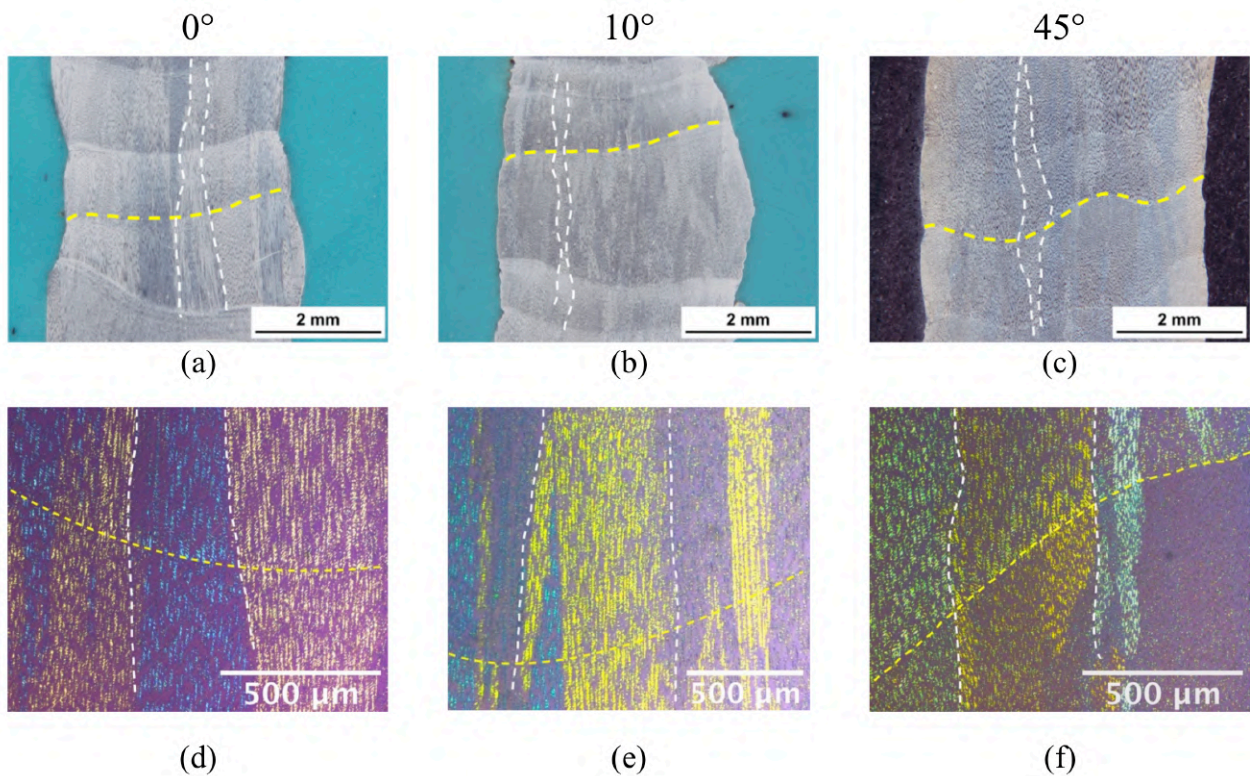


Figure 5: Schaeffler Diagram (adapted from [60]): in the diagram, red dashed lines outline the  $Cr_{eq}$  and  $Ni_{eq}$  values obtained from the chemical composition evaluated on WAAM bars leading to the Austenite + Ferrite (A+F) region

#### 4.2 Microstructural characterization

As mentioned before, the dot-by-dot methodology involves the subsequent deposition of single metal droplets that rapidly solidify on the previously deposited material, thus forming the layered microstructure typical of additive manufacturing. Low magnification metallographic analyses (Figure 6) give a general view of the microstructure of WAAM bars, in which evidence of the droplet deposition can be found. In particular, by comparing the representative longitudinal sections taken along the  $z$ -axis of dot-0, dot-10 and dot-45 bars (Figures 6a,b and c), layers formed by the subsequent depositions, whose boundaries are underlined in yellow in the figure, can be seen. In case of dot-0 and dot-10 (Figures 6a,b), layer boundaries are almost perpendicular to the building direction while a slight inclination can be observed for dot-45 bars (Figure 6c). The analyses also evidenced the variability in the bar diameter that will be further addressed in the following section. It is well-documented in the literature that additive processes, like WAAM, often lead to epitaxial grain growth [61]. Due to epitaxy, during the solidification of molten droplets grains grow directly from the previously deposited layer, replicating the same crystallographic orientation and following the maximum thermal gradient. Therefore, the formation of highly-oriented large columnar grains crossing-over layers is promoted. Evidence of this is given in Figures 6d,e,f, where the observation

of metallographic sections under polarized light allows to outline epitaxial columnar grains. In the figures, the focus is given to the interlayer region of bars, showing large grains (white dashed lines) that cross-over the layer boundary (yellow dashed lines) without changing their crystallographic orientation. For all the three investigated build angles ( $0^\circ$ ,  $10^\circ$  and  $45^\circ$ ), epitaxial grains followed the direction of longitudinal axis of bars ( $z$ -axis). In fact, a similar grain orientation was observed for dot-0, dot-10 and dot-45 bars, thus showing no remarkable influence from the different build angles, even if the layer boundaries were almost perpendicular to the  $z$ -axis in case of dot-0 and dot-10 bars and approximately  $45^\circ$  oriented in case of dot-45 bars.



1  
2 *Figure 6: Representative low magnification microstructural images taken along the longitudinal axis ( $z$ -axis)*  
3 *of the WAAM bars: a, b, c) 3D optical microscopy showing the overall microstructure, d), e), f) color*  
4 *microscopy showing epitaxial growth of columnar grains crossing-over layers. Yellow and white dashed*  
5 *lines underline layer boundaries and epitaxial grains, respectively.*

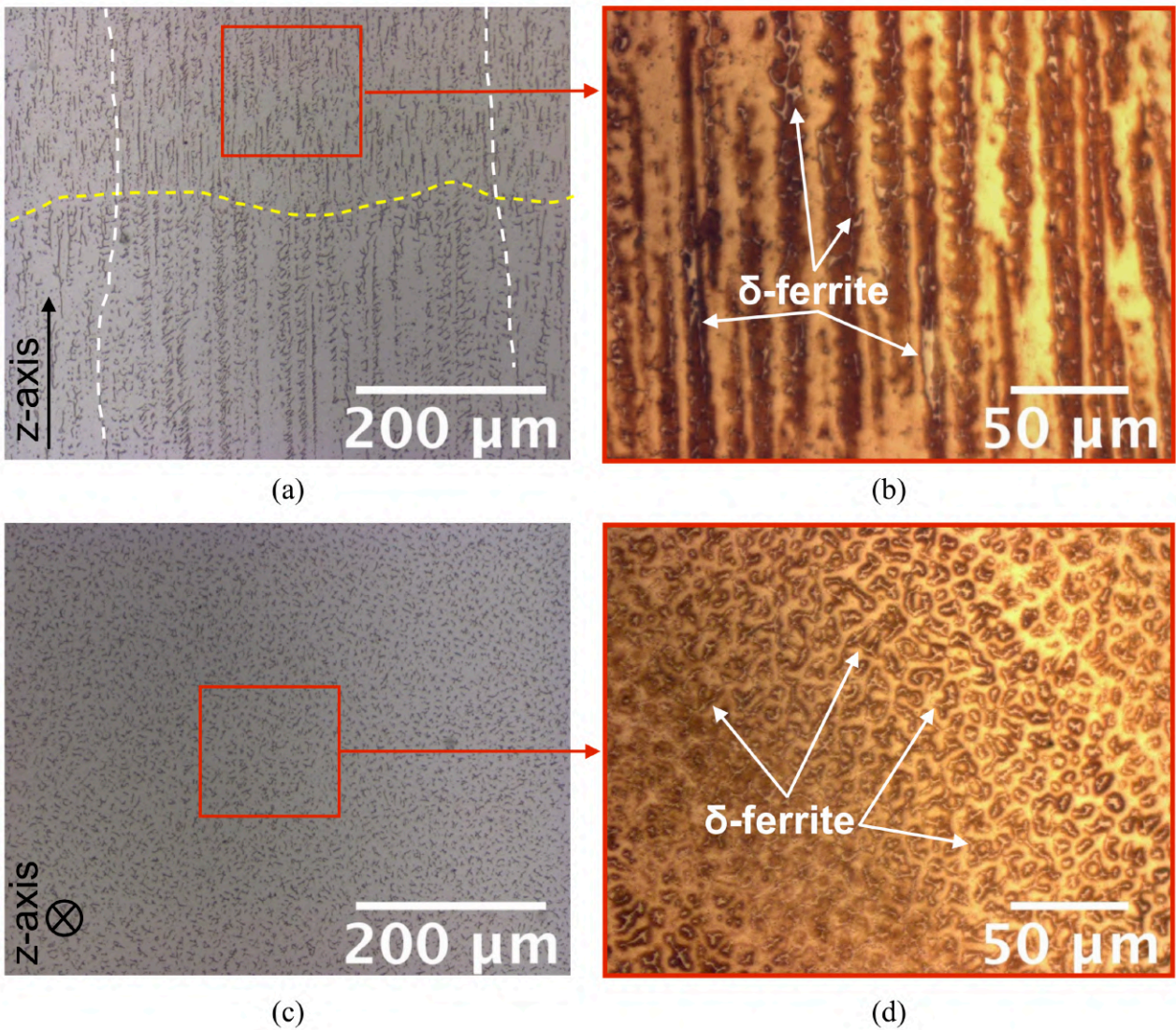
Detail of the solidification structure formed within the large epitaxial grains is given in Figure 7, that compares representative longitudinal and transversal metallographic sections. A fine columnar-dendritic structure can be found inside the long epitaxial grains, for all the investigated build angles. By focusing on the longitudinal sections (Figure 7a,b), it is possible to observe that the columnar dendritic structure is still oriented along the  $z$ -axis, thus following the same direction as the epitaxial

grains. Similar outcomes were already discussed in a previous paper focusing on WAAM plates [38]. As a consequence of the highly oriented microstructure observed along the longitudinal direction, in the transverse one a homogeneous dendritic structure, with no evidence of preferred orientation, can be resolved (Figures 7c,d).

Two main phases were detected and, based on previous analyses on WAAM plates [38,42] and on the chemical composition of bars (Table 2 and Figure 5), they were identified as:  $\gamma$ -austenite and minor  $\delta$ -ferrite, the latter located in the interdendritic regions of  $\gamma$ -austenite. According to the ternary Fe-Cr-Ni phase diagram, in fact, a type ferrite-austenite (FA) solidification is expected. In this view, a specific colour etching [55] was used to reveal the presence of  $\delta$ -ferrite in the austenite matrix (Figure 7b,d). The analysis confirmed the presence of vermicular  $\delta$ -ferrite (white phase in Figure 7b,d) in the interdendritic regions of the  $\gamma$ -austenite, being the predominant phase. The microstructure of all the investigated samples was also analyzed at high magnification by FEG-SEM (Figure 8). FEG-SEM observations confirmed the presence of vermicular  $\delta$ -ferrite inside the  $\gamma$ -austenite. Phases are highly oriented, in the longitudinal section (Figure 8a), along the z-axis. The  $\delta$ -ferrite phase was also observed in the transverse sections (Figure 8b), showing, as already discussed, a non-preferred orientation. High magnification analyses also disclosed globular micrometer-sized particles, whose EDS semi-quantitative analyses revealed the presence of O, Mn, S and Si (Figure 8c). Globular nonmetallic phases in titanium-free cast austenitic stainless steels are reported in the literature, present as complex oxygen compounds [62] whose size decrease with increasing cooling rate [63]. Even if in the WAAM process the molten area is shielded with a flux of inert gas, it is possible that minor oxidation phenomena still occur, as recently demonstrated in case of highly reactive materials as Al and Ti alloys [64,65]. The same particles were also observed on the fracture surface of all samples, as discussed in the following Section 3.5. High magnification analyses also revealed a spread spherical micro-porosity in the samples that can be related to both gas occlusion occurring during the WAAM process and, to some extent, to the metallographic preparation that promoted the detachment of the aforementioned non-metallic inclusions from the matrix.

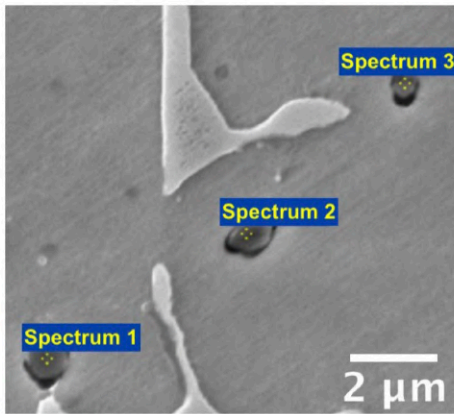
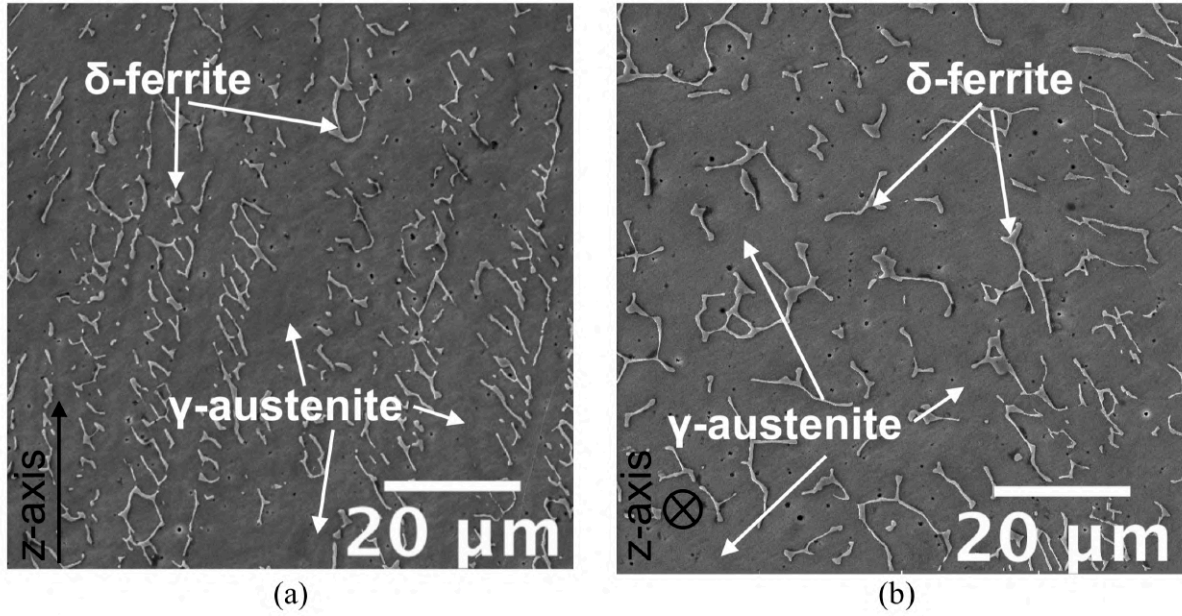
It should be also noticed that in correspondence of the layer boundaries, a discontinuity in the columnar-dendritic structure exists. In fact, due to the complex thermal cycles involved in the deposition of each layer (or droplet), coarsening of the underneath solidified material occurs. By focusing on the micrographs in Figure 6a that shows an interlayer region, it can be seen that in the region immediately above the layer boundary (yellow dashed line) a finer structure can be observed, while in the region below the boundary the structure is coarser. This outcome was observed in correspondence of each layer boundary, regardless the different build angle. Furthermore, analogous

results, in case of WAAM plates, was also discussed in the literature [4,66] and in a previous work [42].



1  
2  
3  
4  
5

Figure 7: Representative optical micrographs of the WAAM bar: a), b) longitudinal sections; c), d) transverse sections. In a) and c) the darker phase is  $\delta$ -ferrite while the lighter one is the  $\gamma$ -austenite. A specific color etching was applied in b) and d) to reveal the  $\delta$ -ferrite as the white phase. Yellow and white dashed lines underline layer boundaries and epitaxial grains, respectively.



Element	Wt.%		
	Spectrum 1	Spectrum 2	Spectrum 3
C	3.64	3.53	5.40
O	12.28	13.82	2.29
Si	6.54	7.46	1.10
S	1.50	0.13	6.33
Cr	14.43	15.68	16.27
Mn	10.30	8.85	10.86
Fe	45.26	45.05	50.08
Ni	6.05	5.48	7.67

(c)

Figure 8: Representative FEG-SEM micrographs of the WAAM bar: a) longitudinal section; b) transverse section; c) EDS analyses performed on inclusions. In the micrographs, the lighter phase is  $\delta$ -ferrite while the darker one is the  $\gamma$ -austenite, as indicated by arrows.

### 4.3 Geometrical characterization

#### 4.3.1 Specimen-to-specimen variability

In order to evaluate the effective mechanical properties for structural design purposes, the volume-equivalent cross-section was assumed as the resistant effective cross-sectional area for the calculation of the effective stresses from tensile tests, according to the procedure adopted also in [37,67].

The average effective diameters  $d_{eff}$  were equal to (Table 3): 5.92 mm for dot-0 specimens (corresponding to a reduction of less than 5% from the nominal diameter, equal to 6 mm), 5.71 mm



1 for dot-10 specimens (corresponding to a reduction of around 5% from the nominal diameter), and  
 2 6.40 mm for dot-45 specimens (corresponding to an increase of around 7% from the nominal  
 3 diameter). For all of them, the coefficient of variation of the effective diameter was of around 5%.  
 4 These results are also in line with the measured diameters of WAAM steel bars studied by Silvestru  
 5 et al. [35], that registered standard deviation values of around 0.20 mm.

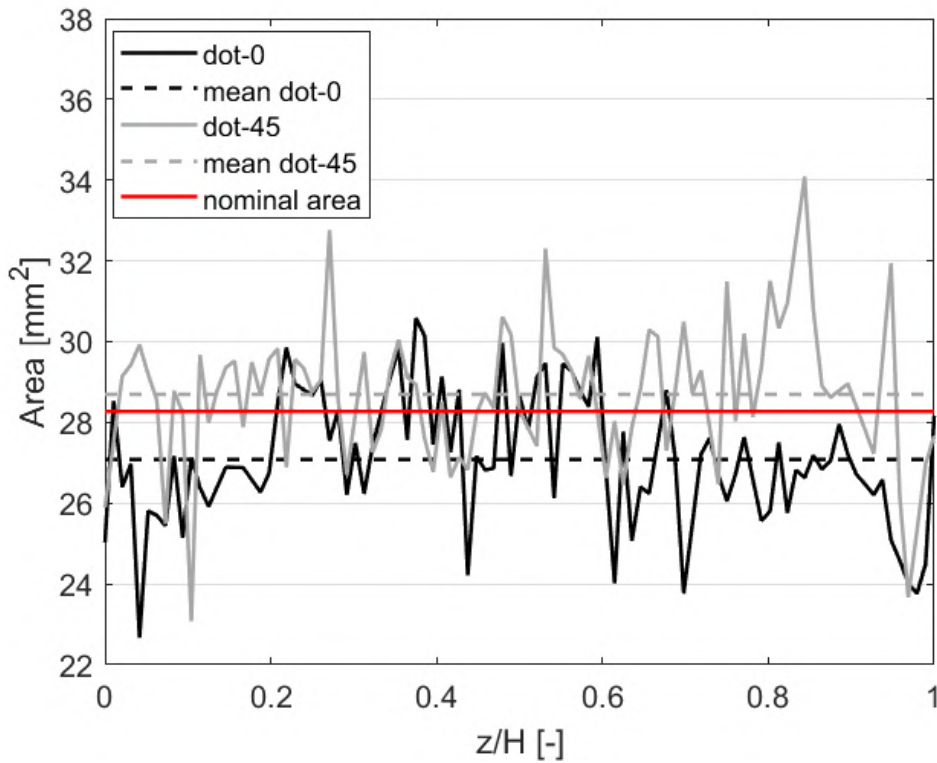
6  
 7 *Table 3: Mean values and standard deviations of diameters for the bars tested: specimen-to-specimen*  
 8 *variability (from volume measures on dot-0, dot-10 and dot-45).*

<b>Specimen-to-specimen variability</b>	
<b>Specimen ID</b>	<b><math>d_{eff}</math> [mm]</b>
dot-0	$5.92 \pm 0.29$
dot-10	$5.71 \pm 0.28$
dot-45	$6.40 \pm 0.29$

9  
 10  
 11 *4.3.2 Inherent variability*

12 From 3D scan acquisition, the 3D models of three bars (one dot-0, one dot-10 and one dot-45) were  
 13 analyzed to quantify the variability of the local geometrical parameters as identified in Section 3.4.  
 14 First, it was found that the variability registered for the dot-10 specimen resulted very similar to the  
 15 one observed for the dot-0 specimen. For this reason, in the present paragraph only the results related  
 16 to two specimens (one dot-0 and one dot-45) are reported and analyzed.

17 For each specimen, first the distribution of the cross-sectional area was studied with reference of the  
 18 120 sections taken from 3D scan. Figure 9 compares the measured values with the nominal cross-  
 19 sectional area ( $A_n= 28.3 \text{ mm}^2$ ). Overall, the dot-45 specimen presents slightly higher mean value with  
 20 respect to the nominal one, while dot-0 presents a lower mean value. The dot-45 specimen also  
 21 evidences higher scatter in the punctual values (values ranging from 23 to 34  $\text{mm}^2$ ) with respect to  
 22 the dot-0 one (values ranging from 23 to 30  $\text{mm}^2$ ).



1

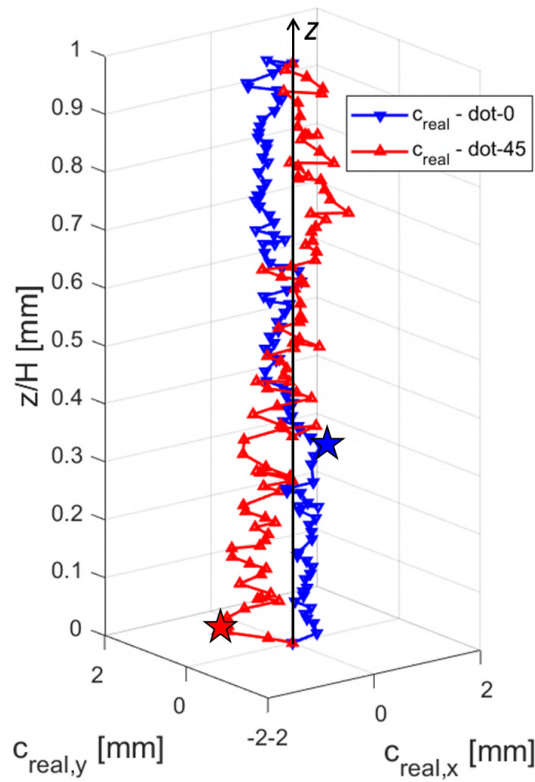
2 *Figure 9: Graphical representation of the variation of the cross-sectional area  $A(z)$  along the longitudinal*  
 3 *axis.*

4 Then, the statistical distribution of the real cross-sectional area was computed and normalized in  
 5 terms of mean value ( $A_{real}(z)/A_{mean}$ ). For both specimens, Normal and Lognormal best-fit distributions  
 6 were also computed. In both cases, the two distributions fit well the data. The standard deviation  
 7 values (which, in case of normalized distributions, correspond to the coefficient of variation) resulted  
 8 equal to 0.06 for both dot-0 and dot-45 bars.

9 The average real diameter  $d_{real}(z)$  resulting from the analysis of the 3D-scan acquisition for the dot-0  
 10 bar resulted equal to 5.87 mm, with a coefficient of variation equal to 3%. Regarding the dot-45 bar,  
 11 the mean diameter resulted equal to 6.05 mm, with a coefficient of variation equal to 3%. Again, the  
 12 results are in line with findings reported in the work by Silvestru et al. [35] which evidenced standard  
 13 deviation values between 0.13 and 0.21 mm (for a nominal diameter of 8 mm).

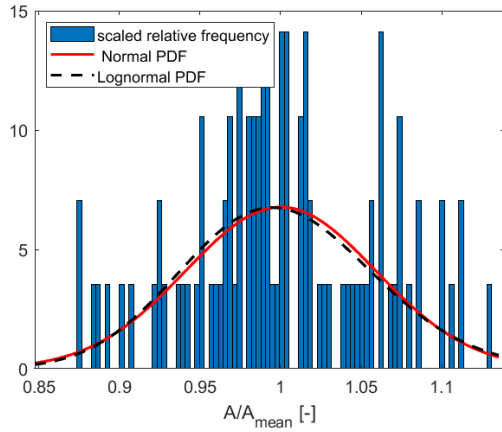
14 The out-of-roundness was estimated by computing the ratio between the real diameter ( $d_{real}$ )  
 15 computed according to Section 3.4 and each of the two dimensions of the circumscribed rectangle  
 16 ( $L_x, L_y$ ). For the dot-0 bar, the average values of the ratios  $L_x/d_{real}$  and  $L_y/d_{real}$  resulted equal to 1.03  
 17 and 0.99, respectively, with a coefficient of variation of 2% for both of them. For the dot-45 bar, the  
 18 average values of the ratios  $L_x/d_{real}$  and  $L_y/d_{real}$  resulted equal to 1.01 and 1.00, respectively, with a  
 19 coefficient of variation of 2% for both of them. Thus, the results confirmed that the real cross-sections  
 20 can be approximated to a circular shape.

1 Figure 10a displays the real longitudinal axis of the two WAAM bars, i.e. dot-0 (blue line) and dot-  
 2 45 (red line). The eccentricity ( $e$ ) of the bars were computed in terms of modulus of the coordinates  
 3 of the real centroid  $C_{real}(z)=(C_{real,x}, C_{real,y})$  as follows:  $e = \sqrt{C_{real,x}^2 + C_{real,y}^2}$ .  
 4 For the dot-0 bar, the mean value ( $e_{mean}$ ) and standard deviation ( $\sigma_e$ ) of  $e$  (over a height of 250 mm)  
 5 resulted equal to  $e_{mean} = 0.43$  mm and  $\sigma_e = 0.23$  mm (coefficient of variation of 0.53), with a  
 6 maximum value equal to  $e_{max} = 0.92$  mm (for a ratio  $e_{max}/H$  equal to 0.46%). For the dot-45 bar, the  
 7 mean value and the standard deviation of  $e$  (over a height of 200 mm) resulted equal to  $e_{mean} = 0.55$   
 8 mm and  $\sigma_e = 0.26$  mm (coefficient of variation of 0.48), with  $e_{max} = 1.12$  mm (for a ratio  $e_{max}/H$  equal  
 9 to 0.58%). The comparison of values of the three main descriptors of the eccentricity (i.e.  $e_{max}$ ,  $e_{mean}$ ,  
 10  $\sigma_e$ ) indicates that the dot-45 bar has higher irregularity (+15-30%) with respect to the dot-0. Similar  
 11 findings were also reported in the work by [35] which evidenced a much rougher surface in case of  
 12 45° built angle. The larger irregularity of the dot-45 bar could have a detrimental effect on the  
 13 mechanical parameters of bars printed with higher build angles. The values of  $e_{max}$  for the investigated  
 14 dot-0 and dot-45 specimens are also indicated in Figure 10a with a star.  
 15

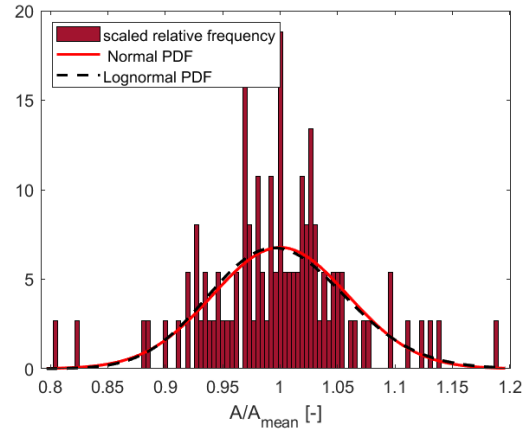


(a)

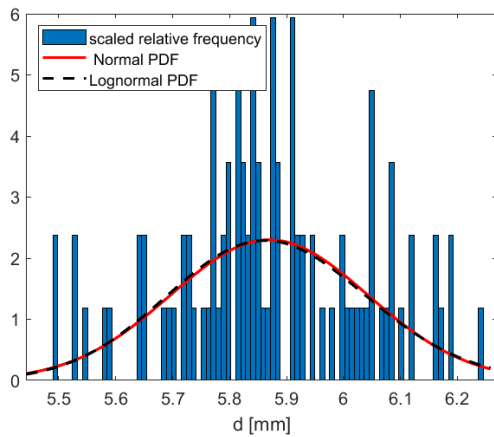
16  
 17



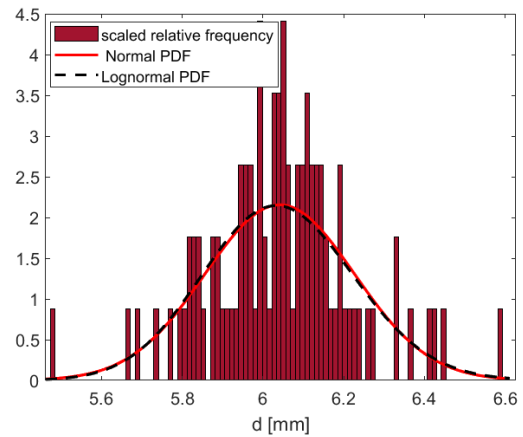
(b)



(c)



(d)



(e)

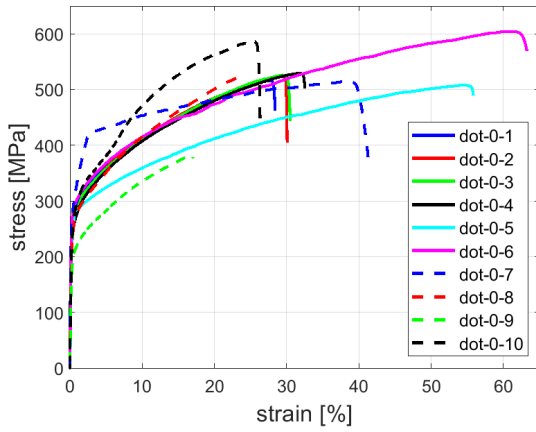
Figure 10: Geometrical characterization of WAAM bars printed with different build angles: (a) comparison of longitudinal eccentricity (blue – dot-0, red – dot-45); frequency distribution of normalized cross-sectional area (b) for dot-0, (c) for dot-45; frequency distribution of diameters (d) for dot-0 (e) for dot-45.

#### 4.4 Tensile and hardness data

The tensile tests were performed on a total of 29 specimens (10 dot-0 specimens, 10 dot-10 specimens and 9 dot-45 specimens). Figure 11 presents the effective stress-strain curve of WAAM bars and a zoom of them (for strain values lower than 1% and stress values lower than 400 MPa). Effective stress values  $\sigma_{eff}$  were computed as the ratio between the tensile force acting on the specimen and its effective cross-sectional area (according to Eq.1). Effective strains were computed according to Eq. 2 and considering a gauge length of 50 mm. Overall, for all three inclinations considered, a significant inherent variability in the tensile response can be detected for each single orientation. Dot-0 and dot-10 specimens presented ultimate tensile strength values up to 600 MPa and elongation to failure up to 40%. On the other hand, dot-45 specimens presented ultimate tensile strength values up to 480 MPa and elongation to failure values up to 35%. All three orientations registered very large

1 post-yielding hardening behavior until rupture. From a closer look at the first part of the tensile tests  
2 (deformation values less than 1%) (Figures 11 b,d,f), the 0.2% proof stress values were around 200-  
3 250 MPa for all three inclinations.

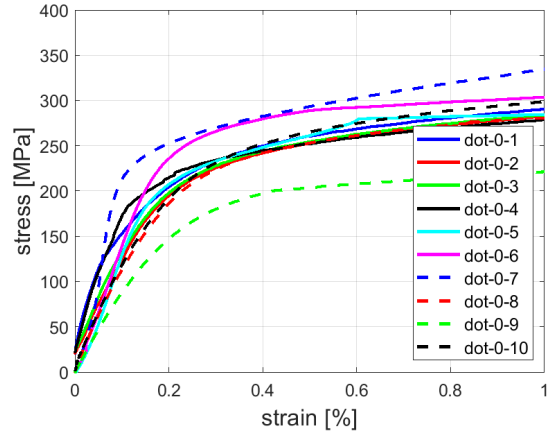
4



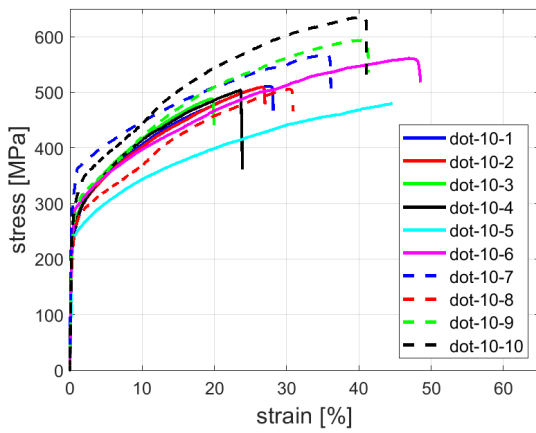
5

6

(a)



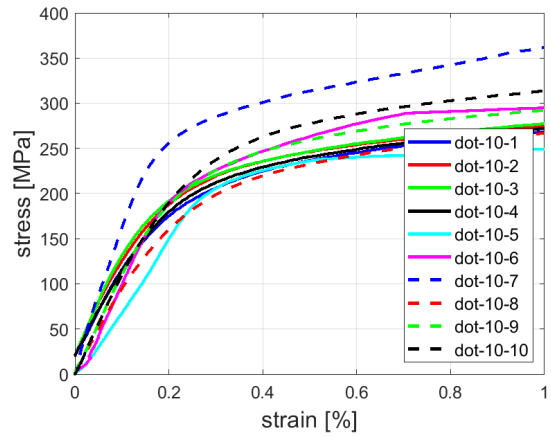
(b)



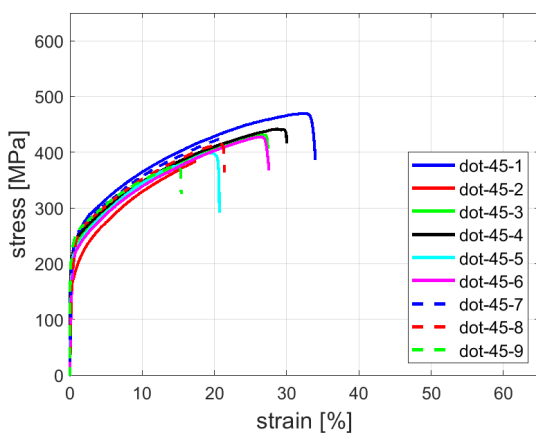
7

8

(c)



(d)

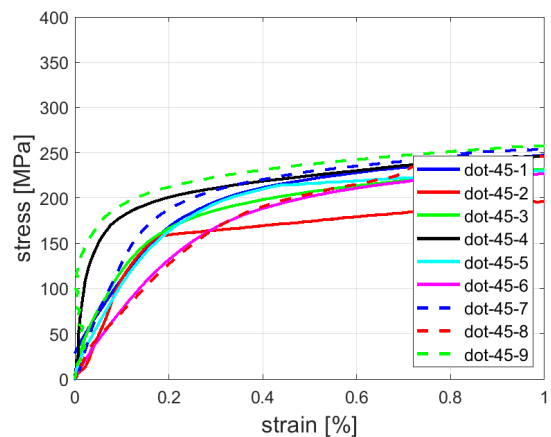


9

10

11

(e)



(f)

Figure 11: Effective stress-strain curves for tensile tests on WAAM bars: full curve and a zoom of them (up to 1% strain) for specimens with (a,b) dot-0, (c,d) dot-10 and (e,f) dot-45.

Table 4 collects the values of the key effective mechanical parameters (means +/- standard deviations), in terms of Young's modulus ( $E$ ), 0.2% proof stress ( $R_{p,0.2}$ ), ultimate tensile strength ( $UTS$ ) and elongation to failure ( $A\%$ ) according to ISO 6892-1 [57]. Values of yield-to-tensile strength ratio

( $R_{p0.2}/UTS$ ) and element's ductility ( $\mu_e = \frac{\epsilon_{eff,u}}{\epsilon_{eff,Rp02}} = \frac{A\%}{\epsilon_{eff,Rp02}}$ ) are also reported. In order to accurately

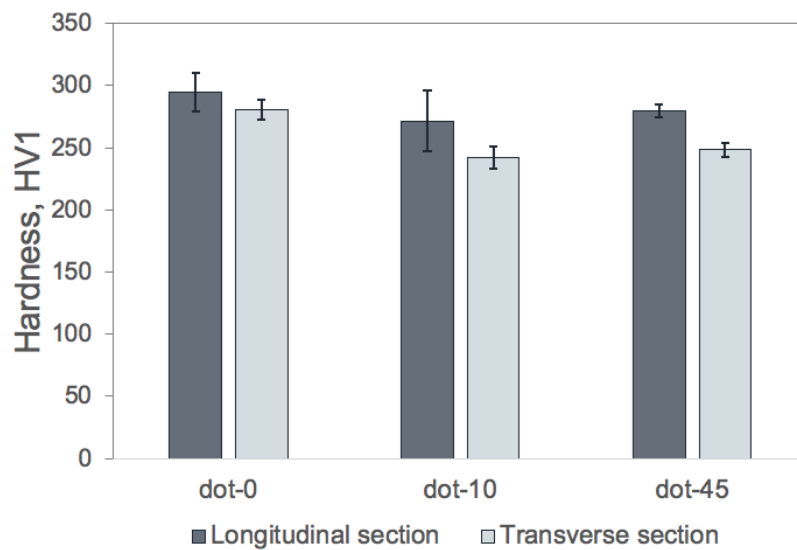
evaluate the Young's modulus values overcoming the experimental noise typical of the effective stress-strain curves, an ordinary least squares regression (OLSR) analysis was employed, as proposed by [67] and also adopted in [25,40].

Table 4: Key effective mechanical parameters from tensile tests on WAAM bars.

Specimen ID	E [GPa]	R <sub>p0.2</sub> [MPa]	UTS [MPa]	A% [%]	R <sub>p0.2</sub> /UTS [-]	μ <sub>e</sub> [-]
dot-0	133 ± 27	243 ± 20	524 ± 56	35 ± 14	0.47 ± 0.03	93 ± 42
dot-10	108 ± 19	245 ± 21	536 ± 49	34 ± 9	0.46 ± 0.03	79 ± 21
dot-45	98 ± 28	208 ± 20	419 ± 29	24 ± 6	0.50 ± 0.05	55 ± 14

Overall, the average value of all the key effective mechanical parameters decrease with increasing build angle. As far as Young's modulus is concerned, the specimens present significantly low values (between 100 and 140 GPa) with a very large scatter. Values of 0.2% proof stress and ultimate tensile strength are instead comparable to the standard values for structural steel. Elongation at rupture values are between 25% and 35% with very large scatter for all three build angles. The ductility of the element has values ranging between 50 to 100 with, again, very large scatter for all three build angles. Hardness results ( $HV_1$ ) are reported in Figure 12, as average values measured on the longitudinal and transverse metallographic sections of all investigated build angles. By considering standard deviations, hardness evaluated on longitudinal sections (along z-axis), thus parallel to the tensile load direction, can be considered comparable among dot-0, dot-10 and dot-45 bars. On the other hand, for all build angles tested, hardness measured on transverse section (perpendicular to the z-axis) was

1 lower than longitudinal one. The slight difference between the longitudinal and transverse sections is  
 2 possibly related to the difference in the microstructural features discussed in Section 4.2. Specifically,  
 3 both optical and FEG-SEM microscopy showed an anisotropy in the microstructure due to the  
 4 additive process, evident if the morphology of the  $\delta$ -ferrite (whose hardness and strength are slightly  
 5 higher than austenite) is concerned. Furthermore, a modest decrease in the average hardness value  
 6 was observed for bars printed with  $10^\circ$  and  $45^\circ$  build angle, if compared to  $0^\circ$  ones. Consequently,  
 7 the overall hardness of  $0^\circ$  bars (287 HV<sub>1</sub>) was higher than 10 and  $45^\circ$  ones (257 and 264 HV<sub>1</sub>,  
 8 respectively). However, the difference among the three build angles tested is very narrowed.  
 9



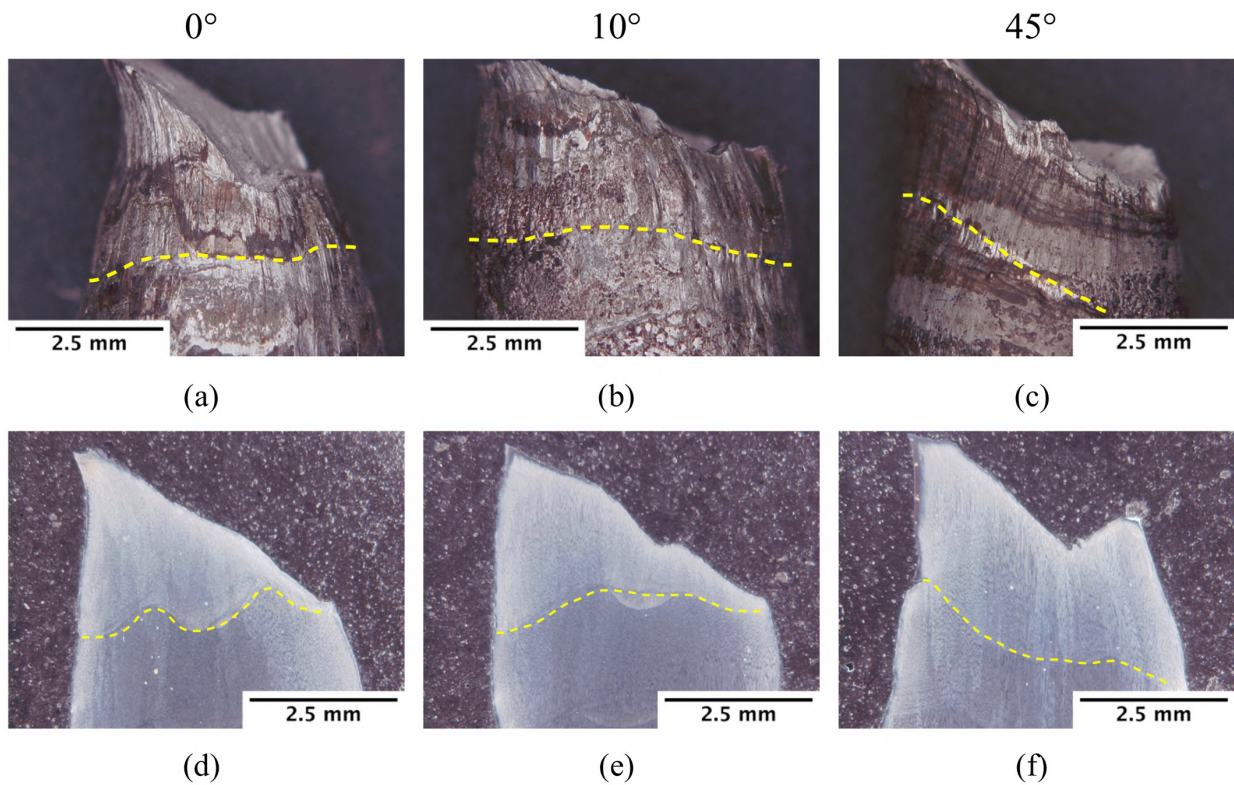
10  
 11 *Figure 12: Hardness measurements. (HV<sub>1</sub>) performed on longitudinal and transverse section of WAAM bars.*  
 12

#### 13 **4.5 Fracture surfaces**

14 Fracture surfaces were initially observed at low magnification by means of a 3D digital  
 15 microscope. In order to delineate the fracture path, micrographs in Figure 13 show the view along  $z$ -  
 16 axis of representative dot-0, dot-10, and dot-45 specimens (Figure 13 a,b,c), and the corresponding  
 17 metallographic sections (Figure 13 d,e,f). From the analyses in Figure 13 it is evident that, for all the  
 18 tested build angles, fracture occurred along a direction inclined by  $45^\circ$  to the applied tensile load (i.e.  
 19 longitudinal  $z$ -axis), consistent with the plane of maximum shear stress. By referring to the layer  
 20 boundaries, underlined by the yellow dashed lines in the figure, dot-45 specimens were characterized  
 21 by the most unfavorably orientation with respect to the plane of maximum shear stress. In fact, as  
 22 also discussed above, the layer boundaries of dot-45 were approximately oriented at  $45^\circ$  to the  $z$ -axis.  
 23 This outcome contributes to further justify the mechanical properties of dot-45 specimens, lower than  
 dot-0 and dot-10 especially in terms of tensile strength and elongation. By recalling the results of

1 microstructural analyses, the interlayer region is characterized by a change in the morphology of the  
 2 columnar dendritic structure, as coarsening of the microstructure occurs due to the deposition of the  
 3 following droplet (Figure 7a). In addition, it can be assumed that minor localized oxidation or  
 4 contamination phenomena occurred, even if the surface of the molten metal is protected by a shielding  
 5 gas during the deposition. This assumption is supported by the globular particles, presumably related  
 6 to non-metallic inclusions, that were detected in the microstructure (Figure 8).

7



8

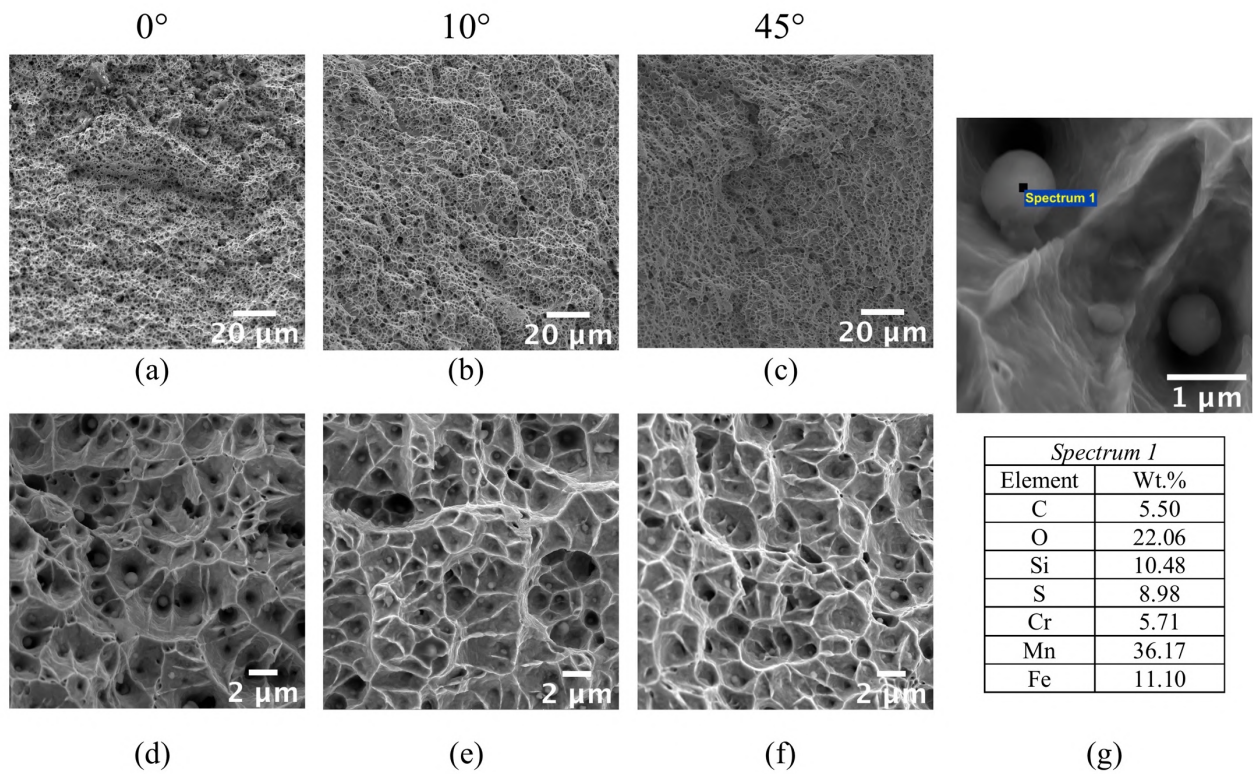
9 *Figure 13: Analyses of fracture surfaces by means of 3D digital microscopy: a), b), c) longitudinal view and*  
 10 *d), e), f) metallographic sections of 0°, 10° and 45° WAAM bars.*

11

12 The same globular particles were markedly detected on fracture surfaces of all samples, suggesting  
 13 that they had a major role in determining the mechanical performances of the WAAM bars. In fact,  
 14 fracture surfaces were observed at both low and high magnification by means of FEG-SEM (Figure  
 15 14). A general view of fracture surfaces can be appreciated in low magnification analyses (Figure 14  
 16 a,b,c), where a ductile fracture characterized by dimples can be observed for all specimens, regardless  
 17 the build angle. A more detailed insight into dimples morphology was obtained at higher  
 18 magnification (Figure 14 d,e,f). As a consequence of the very fine microstructure resulting from the  
 19 WAAM process, dimples size was in the order of few micrometers. No trace of a preferred orientation  
 20 among samples was evidenced. It is known that dimples form due to microvoids nucleation, growth



1 and coalescence in correspondence of hard second phases, such as non-metallic inclusions that  
 2 strongly contribute to the ductile fracture [68]. In fact, globular sub-micrometric particles, consistent  
 3 with the ones observed in Section 4.2, were detected inside dimples on WAAM bars. A detail of a  
 4 globular particle is given in Figure 14g, with the corresponding semi-quantitative chemical analysis  
 5 performed by EDS, that confirmed the presence of O, Mn, S and Si. As already discussed, oxygen  
 6 compounds on fracture surfaces can be related to oxidation phenomena occurring during the WAAM  
 7 process and could indeed justify the lower elongation at fracture exhibited by WAAM bars compared  
 8 to the conventional wrought material, as well as the scatter showed in the elongation results.  
 9



10 *Figure 14: FEG-SEM analyses of fracture surfaces: a), b) c) low and d), e), f) high magnification of dot-0,*  
 11 *dot-10 and dot-45 bars; (g) microanalysis on globular particles (probably oxides) found inside dimples on*  
 12 *the fracture surfaces of WAAM bars.*

13  
 14

## 5. Interpretation of the mechanical response

### 5.1 Variability of the geometrical irregularities

1 Table 5 reports the ratios between the average effective/nominal diameters and cross-sectional areas  
2 ( $d_{eff}/d_n$  and  $A_{eff}/A_n$ ) together with the coefficients of variation of the effective diameters for the  
3 different build angles. The ratios of the diameter values are between 0.95 and 1.07, while the COV  
4 values are equal to 5%, independently from the specific build angle. These results are also in line  
5 with the findings reported by Silvestru et al. [35] which evidenced discrepancies between average  
6 and nominal diameters in the range of +/-5%.

Overall, the detrimental effect of the higher build angles on the geometrical irregularities (as  
estimated for the dot-45 specimens) could be associated to the lower surface tension of the molten  
pool, which is used to counter gravity and thus avoid overhang limitations. Thus, in order to overcome  
this issue, future studies should be devoted to fine tune the process parameters, with specific regard  
to the heat input.

7

8 *Table 5: Variability of the specimen-to-specimen geometrical irregularities (mean and standard deviation).*

	Specimen-to-specimen geometrical variability	
Specimen ID	$d_{eff}/d_n$ [-]	$A_{eff}/A_n$ [-]
dot-0	$0.99 \pm 0.05$	$0.98 \pm 0.10$
dot-10	$0.95 \pm 0.05$	$0.91 \pm 0.09$
dot-45	$1.07 \pm 0.05$	$1.14 \pm 0.10$

9

10 Table 6 summarizes the main results obtained from the inherent geometrical characterization of the  
11 dot-0 and dot-45 3D-scanned bars in terms of: (i) ratios between the real and effective cross-sectional  
12 area ( $A_{real}/A_{eff}$ ) and (ii) diameter ( $d_{real}/d_{eff}$ ), (iii) discrepancy between real and nominal diameter  
13 ( $d_{real}/d_n$ ), (iv) out-of-roundness parameters ( $L_x/d_{real}$  and  $L_y/d_{real}$ ) and (v) lack-of-straightness  
14 parameter ( $e/H$ ). It can be noted that the COV values are around 2-3% for the diameter and out-of-  
15 roundness parameter, around 6% for the cross-sectional area, and around 10-12% for the lack-of-  
16 straightens parameters.

17 The overall variability resulting from specimen-to-specimen and inherent variability is one important  
18 source of variability of the key effective mechanical parameters. For instance, the overall COV of the

1 cross-sectional area can be estimated through the well-known SRSS combination rule, resulting in a  
 2 value of around 12%.

In general, the geometrical parameters here studied (i.e. diameter variability, eccentricity) could be used as reference for a methodology aimed at evaluating and further classifying the printing quality of WAAM bars realized by various providers with different sets of process parameters.

3 *Table 6: Variability of the inherent geometrical irregularities (mean and standard deviation)*

Specimen ID	Inherent geometrical irregularities					
	$A_{real}/A_{eff}$ [-]	$d_{real}/d_{eff}$ [-]	$L_x/d_{real}$ [-]	$L_y/d_{real}$ [-]	$d_{real}/d_n$ [-]	$e/H$ [%]
dot-0	0.98 ± 0.06	0.99 ± 0.03	1.02 ± 0.02	0.99 ± 0.02	0.98 ± 0.03	0.22 ± 0.12
dot-45	0.99 ± 0.06	0.99 ± 0.03	1.01 ± 0.03	1.00 ± 0.02	1.01 ± 0.03	0.28 ± 0.10

## 5.2 Variability of the key effective mechanical parameters

6 Table 7 reports the values of the coefficient of variation (COV) registered for the key effective  
 7 mechanical parameters, considering the three different build angles. The values allow to make some  
 8 interesting observation regarding the variability of such parameters. Young's modulus values  
 9 exhibited large COV, in the range of 20-30%. Such values are in line with those exhibited by the as-  
 10 built specimens cut from plates and printed with the same wire [25] and are mainly caused by the  
 11 inherent geometrical irregularities of the specimens (both cross section area and lack of straightness).  
 12 0.2% proof stress and ultimate tensile strength variabilities are between 8-12%. As expected, such  
 13 variability is very close to the overall cross-sectional area variability (COV estimate equal to 12%).  
 14 Elongation at rupture and element's ductility exhibit very large COV values, in the range of 25-45%,  
 15 which are influenced by all the geometrical variabilities. The high sensitivity of these parameters on  
 16 all the geometrical irregularities is in line with the observations provided in Section 2.

17  
 18 *Table 7: Variability of the key effective mechanical parameters (COV).*

Effective mechanical parameter variability
--

Specimen ID	E	R <sub>p0.2</sub>	UTS	A%	μ <sub>e</sub>
dot-0	22%	11%	12%	39%	45%
dot-10	18%	9%	9%	33%	27%
dot-45	28%	8%	7%	26%	26%

1

2 Figure 15 and Table 8 compare the key effective mechanical parameters for the three build angles  
3 investigated on WAAM bars. Reference to traditional values of the key mechanical parameters of  
4 304L stainless steel according to European building code [58] (red dotted line) and the results  
5 obtained for specimens cut transversally from WAAM-produced 304L stainless steel plates  
6 (presented in [38]) are also provided.

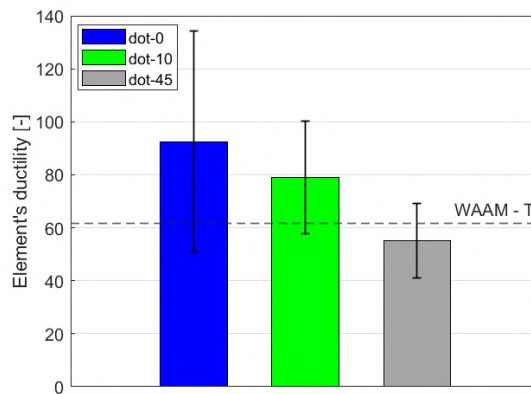
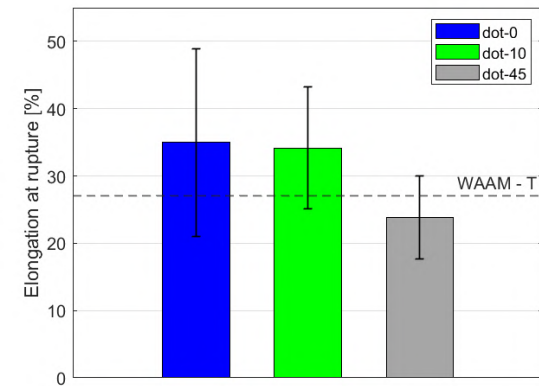
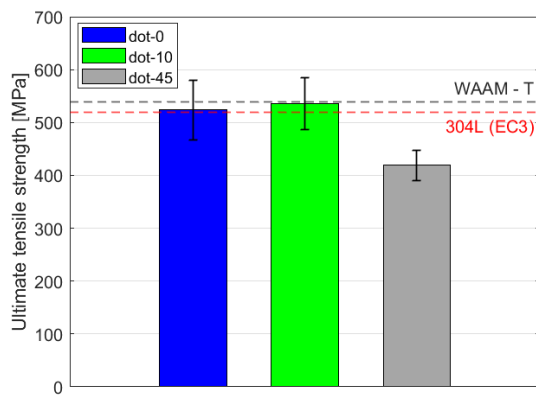
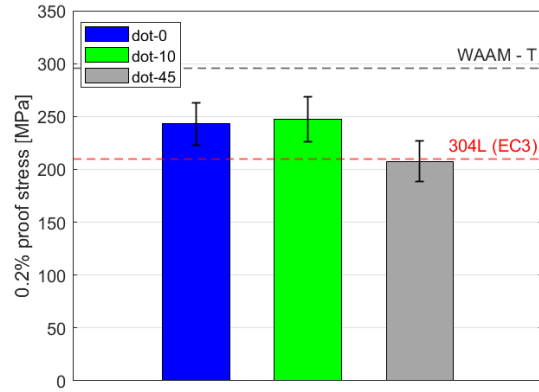
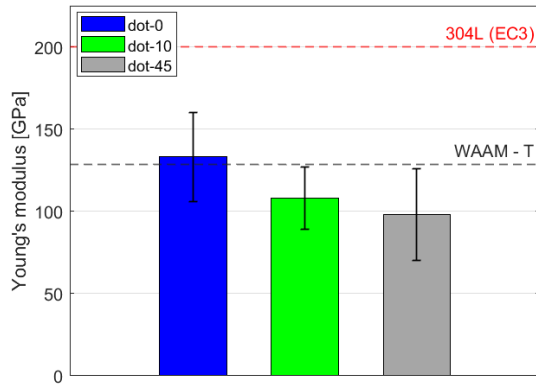
7 Young's modulus values are much lower than the conventional 304L stainless steel (140 to 100 GPa  
8 vs. 200 GPa). Values of 0.2% proof stress are within the ranges provided by Eurocode 3 [58] for  
9 conventional 304L stainless steel. Similar results are registered for ultimate tensile strength values,  
10 with the exception of dot-45 specimens, for which a value of around 420 MPa is computed on average,  
11 lower than the recommended ranges in [58] of 500-520 MPa for 304L steel. The lower tensile strength  
12 of dot-45 specimens can be associated to both the geometrical irregularities (see Section 4.3) and the  
13 unfavorable orientation of the layer boundaries (see Section 4.2) to the tensile load, as also confirmed  
14 by their lower elongation.

15 With reference to the key effective mechanical parameters extracted from WAAM 304L stainless  
16 steel plates (WAAM-T, see e.g. [25,37,38]), the values of Young's modulus and elongation at rupture  
17 are in line with those reported in this study. The low stiffness is indeed related to the texture formed  
18 due to the epitaxial grain growth evidenced by microstructural analysis performed on bars (see  
19 Section 4.2) and investigated more in details on plates (see e.g. [25,42]).

20 On the other hand, 0.2% proof stress values reported for WAAM bars are significantly lower than  
21 WAAM-T (of around 250 MPa vs. 350 MPa). Slightly lower values are also registered for ultimate  
22 tensile strength values (of around 500 MPa vs. 600 MPa).

23 With reference to the elongation and ductility, it should be noticed that a high deviation from the  
24 average value was evidenced. In addition to the previously discussed geometric variability, it should  
25 be also taken into account that the nonmetallic inclusions and microporosities observed during  
26 microstructural and fractographic analyses, strongly influence the mechanical behavior, especially in  
27 terms of ductility and elongation.

28



(e)

Figure 15: Results of the tensile tests on WAAM dot-by-dot bars printed at different angles: (a) Young's modulus; (b) 0.2% proof stress; (c) ultimate tensile strength; (d) elongation at rupture; (e) element's ductility. Reference values for conventional 304L stainless steel (from EC3) and results from WAAM specimens cut transversally from plates (WAAM-T) (Ref. [38]) are also added.

1 From the comparison between the specimens printed with different build angles (as also provided in  
 2 Table 8), overall the specimens printed at low build angles (dot-0 and dot-10) register good strength  
 3 properties (in terms of 0.2% proof stress and ultimate tensile strength) in line with conventional 304L  
 4 stainless steel. Values of Young’s modulus, elongation at rupture and element’s ductility registered  
 5 instead the highest influence of the build angle. The detrimental effect of the higher build angle in  
 6 the elongation at rupture and element’s ductility might be due to the higher geometrical irregularities,  
 7 which could influence the ductile behavior after yielding, as also presented in Section 2.

8

9 *Table 8: Relative ratios of the key mechanical parameters with respect to the build angle.*

	<b>Influence of built angle</b>				
<b>Relative ratio</b>	<b>E</b> [-]	<b>R<sub>p0.2</sub></b> [-]	<b>UTS</b> [-]	<b>A%</b> [-]	<b>μ<sub>e</sub></b> [-]
<b>dot-10/dot-0</b>	0.78	0.98	1.00	1.00	0.85
<b>dot-45/dot-0</b>	0.69	0.82	0.78	0.64	0.59

10

11 All results obtained from the geometrical and mechanical characterization provides a body of  
 12 knowledge that can be then used in further study to calibrate ad-hoc partial factors for the structural  
 13 design of WAAM lattice structures. Clearly each set of partial factors is highly correlated to the  
 14 specific printing process characterized by a given set of printing parameters.

15

## Conclusions

The study presents the first results of an extensive experimental work devoted to assess the mechanical response of stainless steel bars printed with Wire-and-Arc Additive Manufacturing (WAAM). In particular, the work focuses on the mechanical response under tensile loading of as-built bars in terms of effective mechanical parameters, with the aim of studying: (i) the influence of the geometrical irregularities proper of the printing process on the mechanical response under tension, (ii) the effect of increasing build angle in the key effective mechanical parameters. Microstructural analysis and detailed geometrical characterization of selected specimens were also carried out for a better interpretation of the results of the tensile tests.

The main results are summarized as follows:

- Chemical composition of the printed bars complied with the requirements for the AISI 304L austenitic stainless steel.
- Microstructural characterization revealed a microstructure directly affected by the deposition process, consisting of successive layers of solidified material, large epitaxial grains crossing over layers and a fine columnar dendritic substructure within grains. For all build angles ( $0^\circ$ ,  $10^\circ$  and  $45^\circ$ ) grains and substructure were strongly oriented along the longitudinal axis of the bars. On the other hand, the inclination of layer boundaries to the longitudinal axis increased with the build angle, being maximum for the  $45^\circ$  built bars.
- The results of the geometrical characterization through 3D scanning acquisition on the specimens printed with three different build angles (at  $0^\circ$ ,  $10^\circ$  and  $45^\circ$ ) revealed a quite uniform specimen-to-specimen variability of the effective diameters and cross-sectional areas with coefficient of variations of around 5% and 10% respectively, independently from the build angles. On the contrary, a detrimental effect of the build angle is observed in terms of increased lack of straightness when comparing specimens printed at  $0^\circ$  and  $45^\circ$  (+30% on the average value and +15% on the maximum value).
- The results of the tensile tests revealed a significant inherent variability (e.g. for a fixed build angle) of all the key effective mechanical parameters with coefficient of variation values ranging from 10% for the yield and ultimate strength parameters up to 30-40% for the parameters associated to the deformation capacity (Young's modulus, elongation at rupture and ductility). Furthermore, the specimens printed at  $45^\circ$  build angle had reduced values of all the key effective mechanical parameters (-20÷35%) with respect to those printed at  $0^\circ$  or  $10^\circ$ . In particular, severely reduced values of element's ductility and Young's modulus were

registered. Reasonings to this can be found in the higher geometrical irregularities, which alter the mechanical response of bars.

- Detailed inspection of the fracture surfaces revealed a ductile fracture behavior in all the investigated specimens. In addition, fracture occurred along the direction of maximum shear stress, tilted at  $45^\circ$  to the longitudinal axis of bars. In this view, bars printed with a  $45^\circ$  build angles revealed to be the most disadvantaged ones.

Overall, the results show a significant variability of the effective mechanical parameters on the inherent geometrical irregularities with a detrimental effect of large build angles on all the geometrical irregularities (especially the lack of straightness) and on the mechanical behavior. These results confirm the need of ad-hoc calibrated partial safety factors for structural design that could properly account for both the inherent geometrical and mechanical variabilities associated to a specific set of WAAM printing parameters.

In this regard, an improved printing process would lead to reduced geometrical discrepancies and, thus, superior mechanical properties, especially in terms of deformation capacity.



## Acknowledgements

The support of Dutch company MX3D held in Amsterdam is gratefully acknowledged for giving the additive-manufactured elements tested.

## Declarations

### *Funding*

Not applicable.

### *Declaration of Competing Interest*

The authors declare that they have no known competing financial interests or personal relationships that could have appeared to influence the work reported in this paper.

### *Data availability*

The raw/processed data required to reproduce these findings cannot be shared at this time as the data also forms part of an ongoing study.

### *CRedit authorship contribution statement*

Vittoria Laghi: Conceptualization, Methodology, Validation, Investigation, Writing – Original Draft.

1 Michele Palermo: Methodology, Visualization, Writing – Review & Editing.

2 Lavinia Tonelli: Validation, Investigation, Writing – Original Draft.

3 Giada Gasparini: Writing – Review & Editing.

4 Valentina Alena Girelli: Investigation.

5 Lorella Ceschini: Validation, Writing – Review & Editing.

6 Tomaso Trombetti: Supervision.

7

## References

8 [1] K.S. Derekar, A review of wire arc additive manufacturing and advances in wire arc additive  
9 manufacturing of aluminium, Mater. Sci. Technol. (United Kingdom). 34 (2018) 895–916.  
10 <https://doi.org/10.1080/02670836.2018.1455012>.

11 [2] T.A. Rodrigues, V. Duarte, R.M. Miranda, T.G. Santos, J.P. Oliveira, Current status and  
12 perspectives on wire and arc additive manufacturing (WAAM), Materials (Basel). 12 (2019).

- 1 <https://doi.org/10.3390/ma12071121>.
- 2 [3] C. Buchanan, L. Gardner, Metal 3D printing in construction: A review of methods, research,  
3 applications, opportunities and challenges, *Eng. Struct.* 180 (2019) 332–348.  
4 <https://doi.org/10.1016/j.engstruct.2018.11.045>.
- 5 [4] C. V. Haden, G. Zeng, F.M. Carter, C. Ruhl, B.A. Krick, D.G. Harlow, Wire and arc additive  
6 manufactured steel: Tensile and wear properties, *Addit. Manuf.* 16 (2017) 115–123.  
7 <https://doi.org/10.1016/j.addma.2017.05.010>.
- 8 [5] L. Ji, J. Lu, C. Liu, C. Jing, H. Fan, S. Ma, Microstructure and mechanical properties of 304L  
9 steel fabricated by arc additive manufacturing, *MATEC Web Conf.* 128 (2017).  
10 <https://doi.org/10.1051/mateconf/201712803006>.
- 11 [6] A.S. Yildiz, K. Davut, B. Koc, O. Yilmaz, Wire arc additive manufacturing of high-strength  
12 low alloy steels : study of process parameters and their influence on the bead geometry and  
13 mechanical characteristics, (2020).
- 14 [7] P. Moore, A. Addison, M. Nowak-Coventry, Mechanical properties of wire plus arc additive  
15 manufactured steel and stainless steel structures, *Weld. World.* 63 (2019) 1521–1530.  
16 <https://doi.org/10.1007/s40194-019-00775-4>.
- 17 [8] M. Ghaffari, A. Vahedi Nemani, M. Rafieezad, A. Nasiri, Effect of Solidification Defects and  
18 HAZ Softening on the Anisotropic Mechanical Properties of a Wire Arc Additive-  
19 Manufactured Low-Carbon Low-Alloy Steel Part, *Jom.* 71 (2019) 4215–4224.  
20 <https://doi.org/10.1007/s11837-019-03773-5>.
- 21 [9] Y. Fu, H. Zhang, G. Wang, H. Wang, Investigation of mechanical properties for hybrid  
22 deposition and micro-rolling of bainite steel, *J. Mater. Process. Technol.* 250 (2017) 220–227.  
23 <https://doi.org/10.1016/j.jmatprotec.2017.07.023>.
- 24 [10] M. Eriksson, M. Lervåg, C. Sørensen, A. Robertstad, B.M. Brønstad, B. Nyhus, R. Aune, X.  
25 Ren, O.M. Akselsen, Additive manufacture of superduplex stainless steel using WAAM,  
26 *MATEC Web Conf.* 188 (2018) 1–8. <https://doi.org/10.1051/mateconf/201818803014>.
- 27 [11] M. Dinovitzer, X. Chen, J. Laliberte, X. Huang, H. Frei, Effect of wire and arc additive  
28 manufacturing (WAAM) process parameters on bead geometry and microstructure, *Addit.*  
29 *Manuf.* 26 (2019) 138–146. <https://doi.org/10.1016/j.addma.2018.12.013>.
- 30 [12] W. Wu, J. Xue, L. Wang, Z. Zhang, Y. Hu, C. Dong, Forming process, microstructure, and  
31 mechanical properties of thin-walled 316L stainless steel using speed-cold-welding additive  
32 manufacturing, *Metals (Basel)*. 9 (2019). <https://doi.org/10.3390/met9010109>.
- 33 [13] X. Zhang, Q. Zhou, K. Wang, Y. Peng, J. Ding, J. Kong, S. Williams, Study on microstructure

- 1 and tensile properties of high nitrogen Cr-Mn steel processed by CMT wire and arc additive  
2 manufacturing, *Mater. Des.* 166 (2019) 107611.  
3 <https://doi.org/10.1016/j.matdes.2019.107611>.
- 4 [14] M. Rafieezad, M. Ghaffari, A. Vahedi Nemani, A. Nasiri, Microstructural evolution and  
5 mechanical properties of a low-carbon low-alloy steel produced by wire arc additive  
6 manufacturing, *Int. J. Adv. Manuf. Technol.* 105 (2019) 2121–2134.  
7 <https://doi.org/10.1007/s00170-019-04393-8>.
- 8 [15] J. Wang, Z. Pan, Y. Wang, L. Wang, L. Su, D. Cuiuri, Y. Zhao, H. Li, Evolution of  
9 crystallographic orientation, precipitation, phase transformation and mechanical properties  
10 realized by enhancing deposition current for dual-wire arc additive manufactured Ni-rich NiTi  
11 alloy, *Addit. Manuf.* 34 (2020) 101240.
- 12 [16] L. Sun, F. Jiang, R. Huang, D. Yuan, C. Guo, J. Wang, Anisotropic mechanical properties and  
13 deformation behavior of low-carbon high-strength steel component fabricated by wire and arc  
14 additive manufacturing, *Mater. Sci. Eng. A.* 787 (2020) 139514.  
15 <https://doi.org/10.1016/j.msea.2020.139514>.
- 16 [17] B.A. Szost, S. Terzi, F. Martina, D. Boisselier, A. Prytuliak, T. Pirling, M. Hofmann, D.J.  
17 Jarvis, A comparative study of additive manufacturing techniques: Residual stress and  
18 microstructural analysis of CLAD and WAAM printed Ti-6Al-4V components, *Mater. Des.*  
19 89 (2016) 559–567. <https://doi.org/10.1016/j.matdes.2015.09.115>.
- 20 [18] R. Biswal, X. Zhang, A.K. Syed, M. Awd, J. Ding, F. Walther, S. Williams, Criticality of  
21 porosity defects on the fatigue performance of wire + arc additive manufactured titanium alloy,  
22 *Int. J. Fatigue.* 122 (2019) 208–217. <https://doi.org/10.1016/j.ijfatigue.2019.01.017>.
- 23 [19] F. Veiga, A. Gil Del Val, A. Suárez, U. Alonso, Analysis of the Machining Process of Titanium  
24 Ti6Al-4V Parts Manufactured by Wire Arc Additive Manufacturing (WAAM), *Materials*  
25 (Basel). 13 (2020). <https://doi.org/10.3390/ma13030766>.
- 26 [20] C. Zhang, Y. Li, M. Gao, X. Zeng, Wire arc additive manufacturing of Al-6Mg alloy using  
27 variable polarity cold metal transfer arc as power source, *Mater. Sci. Eng. A.* 711 (2018) 415–  
28 423. <https://doi.org/10.1016/j.msea.2017.11.084>.
- 29 [21] E.M. Ryan, T.J. Sabin, J.F. Watts, M.J. Whiting, The influence of build parameters and wire  
30 batch on porosity of wire and arc additive manufactured aluminium alloy 2319, *J. Mater.*  
31 *Process. Technol.* 262 (2018) 577–584. <https://doi.org/10.1016/j.jmatprotec.2018.07.030>.
- 32 [22] Z. Qi, B. Cong, B. Qi, G. Zhao, J. Ding, Properties of wire + arc additively manufactured 2024  
33 aluminum alloy with different solution treatment temperature, *Mater. Lett.* 230 (2018) 275–

- 1 278. <https://doi.org/10.1016/j.matlet.2018.07.144>.
- 2 [23] M. Köhler, S. Fiebig, J. Hensel, K. Dilger, Wire and arc additive manufacturing of aluminum  
3 components, *Metals (Basel)*. 9 (2019) 1–9. <https://doi.org/10.3390/met9050608>.
- 4 [24] J. V. Gordon, C. V. Haden, H.F. Nied, R.P. Vinci, D.G. Harlow, Fatigue crack growth  
5 anisotropy, texture and residual stress in austenitic steel made by wire and arc additive  
6 manufacturing, *Mater. Sci. Eng. A*. 724 (2018) 431–438.  
7 <https://doi.org/10.1016/j.msea.2018.03.075>.
- 8 [25] V. Laghi, M. Palermo, G. Gasparini, V.A. Girelli, T. Trombetti, On the influence of the  
9 geometrical irregularities in the mechanical response of Wire-and-Arc Additively  
10 Manufactured planar elements, *J. Constr. Steel Res.* 178 (2021) 106490.  
11 <https://doi.org/10.1016/j.jcsr.2020.106490>.
- 12 [26] P. Kyvelou, H. Slack, D. Daskalaki Mountanou, M.A. Wadee, T. Ben Britton, C. Buchanan,  
13 L. Gardner, Mechanical and microstructural testing of wire and arc additively manufactured  
14 sheet material, *Mater. Des.* 192 (2020) 108675. <https://doi.org/10.1016/j.matdes.2020.108675>.
- 15 [27] L. Gardner, P. Kyvelou, G. Herbert, C. Buchanan, Testing and initial verification of the world's  
16 first metal 3D printed bridge, *J. Constr. Steel Res.* 172 (2020).  
17 <https://doi.org/10.1016/j.jcsr.2020.106233>.
- 18 [28] T. Feucht, J. Lange, 3-d-printing with steel: Additive manufacturing of connection elements,  
19 *Adv. Eng. Mater. Struct. Syst. Innov. Mech. Appl. - Proc. 7th Int. Conf. Struct. Eng. Mech.*  
20 *Comput.* 2019. (2019) 419–424. <https://doi.org/10.1201/9780429426506-75>.
- 21 [29] T. Feucht, J. Lange, B. Waldschmitt, A.-K. Schudlich, M. Klein, M. Oechsner, Welding  
22 Process for the Additive Manufacturing of Cantilevered Components with the WAAM BT -  
23 Advanced Joining Processes, in: L.F.M. da Silva, P.A.F. Martins, M.S. El-Zein (Eds.),  
24 Springer Singapore, Singapore, 2020: pp. 67–78. [https://doi.org/10.1007/978-981-15-2957-](https://doi.org/10.1007/978-981-15-2957-3_5)  
25 [3\\_5](https://doi.org/10.1007/978-981-15-2957-3_5).
- 26 [30] K. Treutler, V. Wesling, The Current State of Research of Wire Arc Additive Manufacturing  
27 (WAAM): A Review, *Appl. Sci.* 11 (2021) 8619.
- 28 [31] V. Laghi, M. Palermo, G. Gasparini, T. Trombetti, Computational design and manufacturing  
29 of a half-scaled 3D-printed stainless steel diagrid column, *Addit. Manuf.* 36 (2020).  
30 <https://doi.org/10.1016/j.addma.2020.101505>.
- 31 [32] H. Kloft, M. Empelmann, N. Hack, E. Herrmann, D. Lowke, Reinforcement strategies for 3D-  
32 concrete-printing , *Civ. Eng. Des.* 2 (2020) 131–139. <https://doi.org/10.1002/cend.202000022>.
- 33 [33] V. Mechtcherine, R. Buswell, H. Kloft, F.P. Bos, N. Hack, R. Wolfs, J. Sanjayan, B.

- 1 Nematollahi, E. Ivaniuk, T. Neef, Integrating reinforcement in digital fabrication with  
2 concrete: A review and classification framework, *Cem. Concr. Compos.* 119 (2021) 103964.  
3 <https://doi.org/10.1016/j.cemconcomp.2021.103964>.
- 4 [34] J. Müller, M. Grabowski, C. Müller, J. Hensel, J. Unglaub, K. Thiele, H. Kloft, K. Dilger,  
5 Design and Parameter Identification of Wire and Arc Additively Manufactured (WAAM) Steel  
6 Bars for Use in Construction, *Metals (Basel)*. 9 (2019) 725.  
7 <https://doi.org/10.3390/met9070725>.
- 8 [35] V.-A. Silvestru, I. Ariza, J. Vienne, L. Michel, A.M. Aguilar Sanchez, U. Angst, R. Rust, F.  
9 Gramazio, M. Kohler, A. Taras, Performance under tensile loading of point-by-point wire and  
10 arc additively manufactured steel bars for structural components, *Mater. Des.* 205 (2021)  
11 109740. <https://doi.org/10.1016/j.matdes.2021.109740>.
- 12 [36] Z. Yu, Z. Pan, D. Ding, J. Polden, F. He, L. Yuan, H. Li, A practical fabrication strategy for  
13 wire arc additive manufacturing of metallic parts with wire structures, *Int. J. Adv. Manuf.*  
14 *Technol.* (2021). <https://doi.org/10.1007/s00170-021-07375-x>.
- 15 [37] V. Laghi, M. Palermo, G. Gasparini, V.A. Girelli, T. Trombetti, Experimental results for  
16 structural design of Wire-and-Arc Additive Manufactured stainless steel members, *J. Constr.*  
17 *Steel Res.* 167 (2020). <https://doi.org/10.1016/j.jcsr.2019.105858>.
- 18 [38] V. Laghi, M. Palermo, L. Tonelli, G. Gasparini, L. Ceschini, T. Trombetti, Tensile properties  
19 and microstructural features of 304L austenitic stainless steel produced by wire-and-arc  
20 additive manufacturing, *Int. J. Adv. Manuf. Technol.* (2020) 3693–3705.  
21 <https://doi.org/10.1007/s00170-019-04868-8>.
- 22 [39] V. Laghi, M. Palermo, G. Gasparini, M. Veljkovic, T. Trombetti, Assessment of design  
23 mechanical parameters and partial safety factors for Wire-and-Arc Additive Manufactured  
24 stainless steel, *Eng. Struct.* 225 (2020). <https://doi.org/10.1016/j.engstruct.2020.111314>.
- 25 [40] V. Laghi, L. Tonelli, M. Palermo, M. Bruggi, R. Sola, L. Ceschini, T. Trombetti,  
26 Experimentally-validated orthotropic elastic model for Wire-and-Arc Additively  
27 Manufactured stainless steel, *Addit. Manuf.* 42 (2021) 101999.  
28 <https://doi.org/10.1016/j.addma.2021.101999>.
- 29 [41] L. Tonelli, V. Laghi, M. Palermo, T. Trombetti, L. Ceschini, AA5083 (Al–Mg) plates  
30 produced by wire-and-arc additive manufacturing: effect of specimen orientation on  
31 microstructure and tensile properties, *Prog. Addit. Manuf.* (2021).  
32 <https://doi.org/10.1007/s40964-021-00189-z>.
- 33 [42] L. Tonelli, R. Sola, V. Laghi, M. Palermo, T. Trombetti, L. Ceschini, P.L. Ceschini, P.T.

- 1 Trombetti, P. Tomaso Trombetti, Influence of Inter-layer Forced Air Cooling on  
2 Microstructure and Mechanical Properties of Wire Arc Additively Manufactured 304L  
3 Austenitic Stainless Steel, (n.d.). <https://doi.org/10.1002/srin.202100175>.
- 4 [43] C.-H. Jeon, J.-B. Lee, S. Lon, C.-S. Shim, Equivalent material model of corroded prestressing  
5 steel strand, *J. Mater. Res. Technol.* 8 (2019) 2450–2460.
- 6 [44] C.-H. Jeon, C.D. Nguyen, C.-S. Shim, Assessment of mechanical properties of corroded  
7 prestressing strands, *Appl. Sci.* 10 (2020) 4055.
- 8 [45] J. Chi-Ho, L. Jae-Bin, S. Chang-Su, Tensile Test of Corroded Strand and Maintenance of  
9 Corroded Prestressed Concrete Girders, *Int. J. Urban Civ. Eng.* 11 (2017) 1384–1388.
- 10 [46] M. Morgese, F. Ansari, M. Domaneschi, G.P. Cimellaro, Post-collapse analysis of Morandi’s  
11 Polcevera viaduct in Genoa Italy, *J. Civ. Struct. Heal. Monit.* 10 (2020) 69–85.
- 12 [47] G.M. Calvi, M. Moratti, G.J. O’Reilly, N. Scattarreggia, R. Monteiro, D. Malomo, P.M. Calvi,  
13 R. Pinho, Once upon a time in Italy: The tale of the Morandi Bridge, *Struct. Eng. Int.* 29 (2019)  
14 198–217.
- 15 [48] I. Finozzi, A. Saetta, H. Budelmann, Structural response of reinforcing bars affected by pitting  
16 corrosion: experimental evaluation, *Constr. Build. Mater.* 192 (2018) 478–488.
- 17 [49] W. Ramberg, W.R. Osgood, Description of stress-strain curves by three parameters, (1943).
- 18 [50] O. Kammouh, S. Silvestri, M. Palermo, G.P. Cimellaro, Performance-based seismic design of  
19 multistory frame structures equipped with crescent-shaped brace, *Struct. Control Heal. Monit.*  
20 25 (2018) 1–17. <https://doi.org/10.1002/stc.2079>.
- 21 [51] MX3D Webpage, (n.d.). [www.mx3d.com](http://www.mx3d.com).
- 22 [52] Oerlikon, (n.d.). <https://www.oerlikon.com/en/>.
- 23 [53] ASTM E3-11 Standard Guide for Preparation of Metallographic Specimens, *ASTM Int.*  
24 (2011). <https://doi.org/10.1520/E0003-11.2>.
- 25 [54] M. Steels, *Metallography and Microstructures of Stainless steels Maraging steels*, *ASM*  
26 *Handb. V9.* 9 (2004) 1–27. <https://doi.org/10.1361/asmhba0003767>.
- 27 [55] D.W. Hetzner, Etching stainless steels for delta ferrite, *Adv. Mater. Process.* 165 (2007) 33–  
28 34.
- 29 [56] Artec 3D webpage, (n.d.). <https://www.artec3d.com>.
- 30 [57] Metallic materials — Tensile testing — Part 1: Method of test at room temperature Matériaux  
31 métalliques — Essai de traction — Partie 1: Méthode d’essai à température ambiante  
32 COPYRIGHT PROTECTED DOCUMENT, Iso 6892-1. (2009).  
33 <http://files.instrument.com.cn/FilesCenter/20090913/200991371610112081.pdf>.

- 1 [58] European Committee for Standardization (CEN), EN 1993 1-4: Eurocode 3 - Design of steel  
2 structures, part 1-4: General rules, supplementary rules for stainless steel, (2015).
- 3 [59] ASTM A276-16, Standard Specification for Stainless Steel Bars and Shapes, ASTM Int.  
4 (2016) 1–8. <https://doi.org/10.1520/A0276>.
- 5 [60] S. Kou, Post-solidification phase transformations, in: *Weld. Metall.*, 2003.  
6 <https://doi.org/10.1002/0471434027.ch9>.
- 7 [61] A. Basak, S. Das, Epitaxy and Microstructure Evolution in Metal Additive Manufacturing,  
8 *Annu. Rev. Mater. Res.* 46 (2016) 125–149. <https://doi.org/10.1146/annurev-matsci-070115-031728>.
- 9 [62] O.K. Tokovoi, D. V. Shaburov, Nonmetallic phase in austenitic stainless steel, *Steel Transl.*  
10 44 (2014) 875–878. <https://doi.org/10.3103/S0967091214120183>.
- 11 [63] Y. Wang, W. Yang, L. Zhang, Effect of Cooling Rate on Oxide Inclusions During  
12 Solidification of 304 Stainless Steel, *Steel Res. Int.* 90 (2019) 1–10.  
13 <https://doi.org/10.1002/srin.201900027>.
- 14 [64] T. Hauser, R.T. Reisch, P.P. Breese, Y. Nalam, K.S. Joshi, K. Bela, T. Kamps, J. Volpp, A.F.H.  
15 Kaplan, Oxidation in wire arc additive manufacturing of aluminium alloys, *Addit. Manuf.* 41  
16 (2021) 101958. <https://doi.org/10.1016/J.ADDMA.2021.101958>.
- 17 [65] A. Caballero, J. Ding, Y. Bandari, S. Williams, Oxidation of Ti-6Al-4V during wire and arc  
18 additive manufacture, *3D Print. Addit. Manuf.* 6 (2019) 91–98.
- 19 [66] L. Wang, J. Xue, Q. Wang, Correlation between arc mode, microstructure, and mechanical  
20 properties during wire arc additive manufacturing of 316L stainless steel, *Mater. Sci. Eng. A.*  
21 751 (2019) 183–190. <https://doi.org/10.1016/j.msea.2019.02.078>.
- 22 [67] P. Kyvelou, H. Slack, D.D. Mountanou, M.A. Wadee, T. Ben Britton, C. Buchanan, L.  
23 Gardner, Mechanical and microstructural testing of wire and arc additively manufactured sheet  
24 material, *Mater. Des.* (2020) 108675. <https://doi.org/10.1016/J.MATDES.2020.108675>.
- 25 [68] A.L.V. Da Costa E Silva, The effects of non-metallic inclusions on properties relevant to the  
26 performance of steel in structural and mechanical applications, *J. Mater. Res. Technol.* 8  
27 (2019) 2408–2422. <https://doi.org/10.1016/J.JMRT.2019.01.009>.
- 28  
29